SAND2022-4533R
SAND2020-#####X

FY22 Update: Development of Surface Sampling Techniques for the Canister Deposition Field Demonstration

Spent Fuel and Waste Disposition

Prepared for
US Department of Energy
Spent Fuel and Waste Science and Technology
Andrew Knight, Rebecca Schaller, Brendan Nation, Sam Durbin, and Charles Bryan
Sandia National Laboratories

April 15, 2022
Milestone No. M3SF-22SN010208043
SAND2020-xxxxx X

Prepared by
Sandia National Laboratories
Albuquerque, New Mexico 87185 and Livermore, California 94550

Sandia National Laboratories is a multimission laboratory managed and operated by National Technology and Engineering Solutions of Sandia, LLC, a wholly owned subsidiary of Honeywell International, Inc., for the U.S. Department of Energy's National Nuclear Security Administration under contract DE-NA0003525.

SUMMARY

This report describes the proposed surface sampling techniques and plan for the multi-year Canister Deposition Field Demonstration (CDFD). The CDFD is primarily a dust deposition test that will use three commercial 32PTH2 NUHOMS welded stainless steel storage canisters in Advanced Horizontal Storage Modules, with planned exposure testing for up to 10 years at an operating ISFSI site. One canister will be left at ambient condition, unheated; the other two will have heaters to achieve canister surface temperatures that match, to the degree possible, spent nuclear fuel (SNF) loaded canisters with heat loads of 10 kW and 40 kW. Surface sampling campaigns for dust analysis will take place on a yearly or bi-yearly basis. The goal of the planned dust sampling and analysis is to determine important environmental parameters that impact the potential occurrence of stress corrosion cracking on SNF dry storage canisters. Specifically, measured dust deposition rates and deposited particle sizes will improve parameterization of dust deposition models employed to predict the potential occurrence and timing of stress corrosion cracks on the stainless steel SNF canisters. The size, morphology, and composition of the deposited dust and salt particles will be quantified, as well as the soluble salt load per unit area and the rate of deposition, as a function of canister surface temperature, location, time, and orientation. Previously, a preliminary sampling plan was developed, identifying possible sampling locations on the canister surfaces and sampling intervals; possible sampling methods were also described. Further development of the sampling plan has commenced through three different tasks. First, canister surface roughness, a potentially important parameter for air flow and dust deposition, was characterized at several locations on one of the test canisters. Second, corrosion testing to evaluate the potential lifetime and aging of thermocouple wires, spot welds, and attachments was initiated. Third, hand sampling protocols were developed, and initial testing was carried out. The results of those efforts are presented in this report. The information obtained from the CDFD will be critical for ongoing efforts to develop a detailed understanding of the potential for stress corrosion cracking of SNF dry storage canisters.

This page is intentionally left blank.

ACKNOWLEDGEMENTS

This work was funded by the U.S. Department of Energy (DOE), Office of Nuclear Energy Spent Fuel and Waste Deposition Research and Development Program. The authors would like to thank Ned Larson of the DOE:NE for program oversight. In addition, we would like to thank the following Sandians for their contributions: Jessica Faubel for profilometry measurements; Thad Vice and Greg Koenig for surface roughness sample collection, coordinate matching for the photometric map, and mockup weld plate design and fabrication; Jason Taylor for atmospheric exposures; and Ryan Katona for providing thoughtful insights as a technical reviewer.

This page is intentionally left blank.

CONTENTS

LIST OF FIGURES

LIST OF TABLES

ACRONYMS

CDFD	canister deposition field demonstration
CISCC	chloride-induced stress corrosion cracking
DOE	U.S. Department of Energy
DPC	dual-purpose canister
FSAR	final safety analysis report
FY	fiscal year
HAZ	heat affected zone
ISFSI	independent spent fuel storage installation
NRC	Nuclear Regulatory Commission
NUHOMS	NUTECH horizontal modular storage system
PNNL	Pacific Northwest National Laboratory
SCC	stress corrosion cracking
SNF	spent nuclear fuel
SNL	Sandia National Laboratories
SS	stainless steel
TC	thermocouple
WD	working distance

SPENT FUEL AND WASTE SCIENCE AND TECHOLOGY
FY22 UPDATE: DEVELOPMENT OF SURFACE SAMPLING TECHNIQUES FOR THE CDFD

1. INTRODUCTION

This report documents work performed in FY21 and FY22 to develop sampling strategies for the Canister Deposition Field Demonstration (CDFD) project. The primary goal of the CDFD project is to develop a clear understanding of dust deposition and composition over time. This goal is critical for evaluating the potential risk of chloride induced stress corrosion cracking (CISCC) during the dry storage of spent nuclear fuel (SNF), as the accumulation of chloride rich salts over time could eventually lead to the formation of a chloride-rich surficial brine as the canister surface cools. The CDFD campaign is a large-scale demonstration that allows for direct measurement of important parameters for evaluating the risk of CISCC, specifically the brine composition and evolution as a function of time and surface temperature, and the deposited salt load (mass per unit area). For the CDFD project, three canisters within their overpacks will be deployed at a near-marine field site for the purpose of evaluating deposition of dust and salts onto the canister surfaces over time. The canisters will have three heat loads of 0kW (ambient), and 10kW and 40kW to mimic SNF initial load conditions. This will enable the determination of the effects of heating and advective air flow through the overpacks on the deposition rates, and on the characteristics of the deposited materials. The test will be carried out over several years, and periodically (yearly or bi-yearly), the canisters will be extracted, and the surface deposits will be hand sampled. Hand sampling will enable better quantification as there is currently no validated method for robotic sampling. However, access limitations within the overpacks do not allow entry and *in situ* sampling, so the canisters will periodically be removed from the overpacks, and hand sampling will be performed *ex-situ*. This report provides the progress of efforts to develop quantitative, reproduceable, hand sampling techniques for the CDFD canisters.

1.1 Background

The overall CDFD dust sampling strategy is documented in a previous report [1]. The sampling will be carried out on the canister surfaces after the heater power has been cut, and the canisters allowed to cool to ambient temperature. The canisters will be hydraulically pulled from the overpacks onto a transfer skid. Once removed, samples of the surface deposits will be collected by hand. Several different areas on each canister surface will be sampled—nominally, as many as 29 locations on one side and end of each canister (Figure 1). At each location, a 2 x 2 sampling grid will be marked on the canister surface; each square is assumed to be equivalent; the grid will be sampled periodically (on a yearly or bi-yearly basis) over the lifetime of the project. The sampling strategy is discussed in detail in Bryan et al. [1], and is designed to characterize long term dust and salt deposition rates, measuring both interval and cumulative accumulation to evaluate the effects of dust accumulation on the rate of further deposition (Figure 2). A second task will be to evaluate salt and brine evolution (possible degassing or atmospheric exchange reactions) on the heated canister surfaces. Initial testing in support of the hand-sampling procedure was described in the FY21 status report [2], and included development of methods for characterizing canister surface roughness (potentially important metric for dust deposition), and initial evaluation of methods for marking the sampling locations on the canisters.

This report documents further work to develop and test the methods for sampling the canister surface. First, characterization of the canister roughness via surface replicating molds, performed using a method developed over the last year, are presented. Surface roughness can affect surface air flow and dust deposition and may affect the planned sampling strategy if correlations are seen in the early testing.

Second, thermocouple wires, attachments, and spot welds, necessary for heating instrumentation were evaluated. As these are necessary items for the CDFD testing anyway, they are also being proposed as a potential canister marking method for the dust sampling locations. Marking methods tested in FY21 (epoxy paint and a stainless steel (SS) blackening agent) proved ineffective, so the possible use of small spot welds as indexing marks for the sample locations is being considered as an alternative. Specifically, the lifetime and ageing of the thermocouple wires, attachments and spot welds and the potential for enhanced localized corrosion were examined. Finally, a template device for hand sampling the canister surface has been developed, and laboratory testing of the effectiveness of hand sampling surface deposits with a moist sponge was evaluated. Although additional work needs to be done, the overall results suggest this method is effective for hand sampling the canister surfaces.

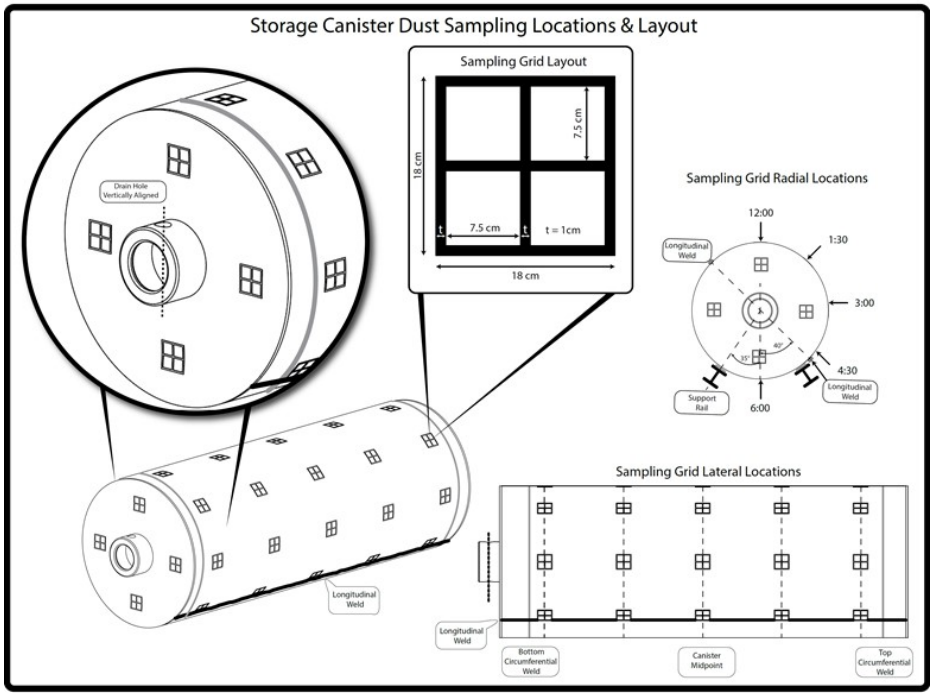

Figure 1. Proposed sampling locations on the canister surface. A total of 25 sampling grids will be used, with 5 circumferential locations at each of the 5 locations along the longitudinal axis of the canister [1].

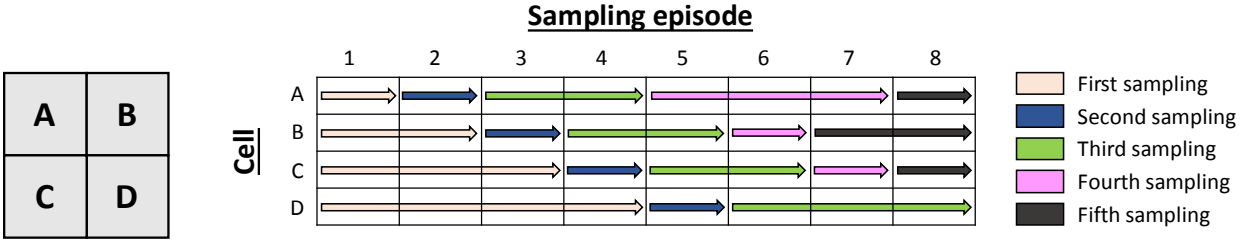

Figure 2. Sampling grid and possible sampling schedule [1].

2. CHARACTERIZATION OF CANISTER SURFACE ROUGHNESS

To gain a better understanding of the canister surface roughness and surface features, two measurement techniques were applied. The canister was mapped using photometric mapping [3] to assess macro-level features. Laser profilometry of surface replicating molds was applied to measure the micro-scale surface roughness. The photometric mapping was completed in 2021 and is described in detail in a previous report by Tanbakuchi, A (2021)[3]. To supplement the photometric mapping, a method to replicate the surface features for profilometric analysis was developed. Conventional surface roughness measurement techniques require the sample be placed on a sample stage in a laboratory, which is not possible for SNF canisters due to their size. Therefore SNL developed a method to "replicate" selected areas of the surface using surface casting materials for profilometric analysis. The goal of this measurement was to provide an estimate of normal surface roughness of the canister (the "mill finish") as well as of selected areas (e.g., ground weld regions and other ground areas) to determine how the surface roughness varies with certain canister features.

2.1 Surface Replicating Methods

2.1.1 Surface Replicating Materials

In FY21 SNL investigated the ability of different mold materials to replicate a metal surface [2]. Briefly, three materials were evaluated for their ability to replicate the surface, including Polytek PlatSil73-25 Silicone Rubber, Polygel Brush-On 35 Rubber, and 3M Express STD VPS Impression Putty. In addition, a thickening agent, PlatThix, and release agent, Pol-Ease 2300, were tested with the Polytek PlatSil73-25 Silicone Rubber and Polygel Brush-On 35 Rubber.

Initial material testing was evaluated based on the ability of the material to replicate the surface (nominally) and its practical usability for the canister surface. The Polytek Brush-on 35 Rubber was not ideal for this application as brushing it on the surface did not successfully replicate the surface – therefore it was not considered further. PlatSil73-25 is a 2-part silicone that, when mixed, formed a viscous fluid that after curing (~5 hours) was easy to remove from the surface, and therefore the release agent (Pol-Ease2300) was not needed. Experiments to determine the impact of the thickening agent on the PlatSil73-25 demonstrated that the more thickening agent used, the softer the resulting surface mold. In addition to softening, the use of PlatThix introduced bubbles into the mold and the number of bubbles increased with increasing volume % of the thickening agent. Overall, PlatSil73-25 performed best when no thickening agent or release agent were added. The last material, 3M Express STD VPS Impression Material Putty, was extremely easy to use, as it could be mixed by hand and cured rapidly (~5 mins). The putty was then pressed onto the surface and allowed to cure. After curing, the 3M Express STD VPS was easy to remove from the surface. Following initial testing, two materials were considered for further analysis: PlatSil 73-25 silicone rubber (Polytek) and Express STD VPS impression Material Putty (3M). However, initial profilometry measurements indicated that micro-scale bubbles formed in the Express STD VPS Impression Material Putty, impacting the quality of the mold, so it was eliminated from consideration. The material selected to determine the surface roughness of the canister was the PlatSil73-25 because it was relatively easy to use and was very effective at replicating the surface.

2.1.2 Sample Cell

In FY21, a sample cell was designed to adhere to the canister surface so that any location could be sampled [2]. Based upon the surface features of interest for this sampling, the sample cell window was created to be 25.4 mm (1 inch) in diameter. This allowed for profilometry methods to determine micron-sized features by measuring several locations across the molded surface. A SOLIDWORKS® drawing of the sample cell is shown in Figure 3. For operation, an adhesive gasket was used to adhere to sampler to the canister surface; then, the PlatSil73-25 silicone rubber was mixed and transferred to a 10 mL syringe. The syringe was connected to the sample cell inlet via tubing, and the silicone rubber was injected into the sample cell until it filled the sample cell and a small amount escaped through the air vent. The sample

cell, filled with the surface replicating material, was allowed to cure (~24 hours). Once cured, the adhesive gasket and sample cell were carefully peeled off the metal surface and the solidified silicone rubber puck with a negative replica of the surface was extracted for analysis (Figure 4).

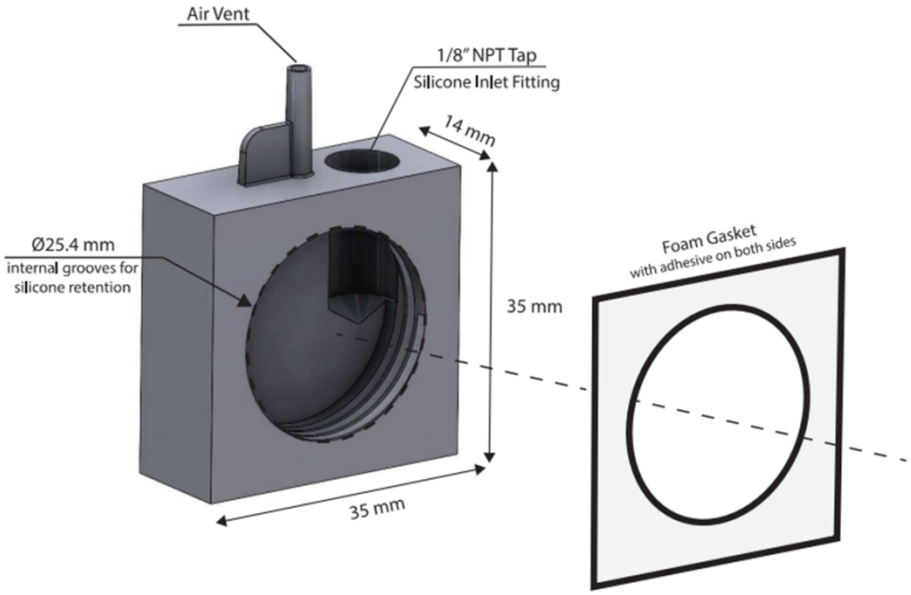

Figure 3. Solidworks rendering of the surface replicator cell showing the features and dimensions.

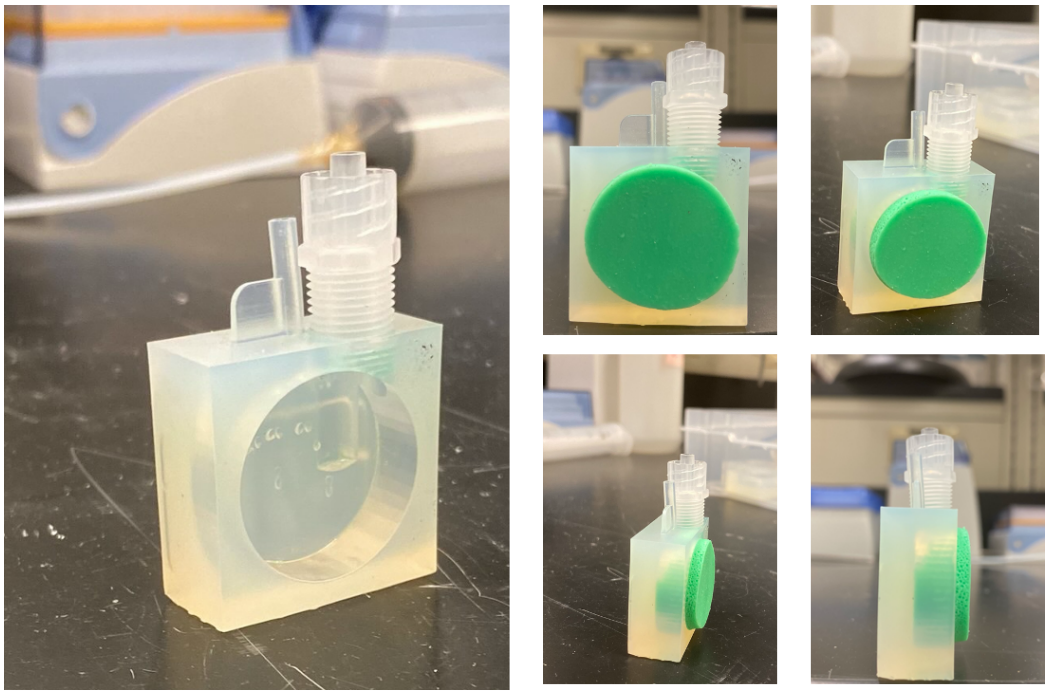

Figure 4. Images of the surface roughness sampling cell. Shown empty (left) and with PlatSil 73-25 silicone rubber following 24 hours of curing on a SS surface.

2.1.3 Profilometry

The surface roughness was measured using a Keyence VK-X150 Laser Scanning Microscope. For each sample, a stitched image was acquired using a 50x standard working distance (WD) objective to create analysis regions of ~550 µm x 755µm for molded samples (Section 2.3) or 3000 µm x 200 µm for unidirectional surface roughness standards (Section 2.2). To determine the size of larger features (e.g., pits), a 10x standard WD objective was used. For noise reduction, images were plane leveled and a medium height cut was applied prior to analysis to minimize the impact of long range surface deviations. An average of 11-line profiles were collected across the image in both directions, and reported surface roughness was from the direction where the roughness was largest, and the standard deviation was smallest (Figure 5).

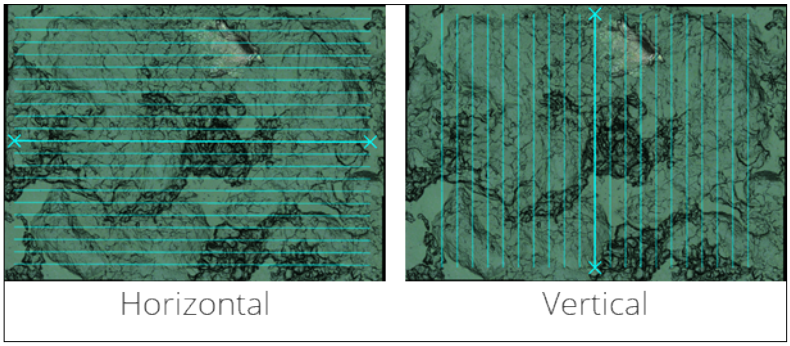

Figure 5. Example of horizontal and vertical line scans used on a sample to obtain the surface roughness.

The line scans were averaged to determine the R_a and R_z for each sample. R_a represents the arithmetic mean of the absolute surface roughness [4-6], calculated by:

$$R_a = \frac{1}{l}\int_0^l |z(x)|dx \qquad eq\ (1)$$

Where l is the length of the line scan, and |z(x)| is the absolute value of the surface topography as a function of position in the x direction. R_z is the deviation between the highest peaks to the lowest valley on the surface [4, 6]. This is calculated by:

$$R_z = R_P + R_V \qquad eq\ (2)$$

Where R_P is the height of the peak and R_v is the depth of the valley. Long range waviness was removed using an automatic tilt correction value of Λ_c = 0.025 mm and was applied to all samples.

2.2 Surface Roughness Standard Measurement

Stainless steel (SS) surface roughness standards were used to validate the effectiveness of the Plat-Sil 73-25 at replicating a surface of known roughness. The surface roughness standards used for this validation were Microsurf 326 (Linishing) and Microsurf 315 (Surface Grinding). Two test areas on each standard were replicated corresponding to an ISO surface roughness of N3-N8. The select areas were chosen to represent the roughness range expected for the canister surface, from0.1 µm < R_a < 3.2 µm and 0.90 µm < R_z < 18.5 µm.. For each region, a surface mold replicate was taken using the sampling cell and the Plat-Sil73-25, then the SS standard and the molds were analyzed via laser profilometry. The tolerances of the surface roughness standards were not reported, so the mold validation was performed by comparing the measured surface roughness via profilometry to the measured mold roughness of the corresponding location.

The 3-D topographic maps of the surfaces are shown in Figure 6, with the mold on top of the corresponding surface roughness standard. Visually, it is clear that the mold effectively creates a negative imprint of the roughness standard surface. Figure 7 shows the measured mold R_a and R_z values versus the measured R_a and R_z values of the surface roughness standard with a 1:1 line. Overall, the measured surface roughness of the mold accurately reflects the surface roughness standards. For R_a all the data points fall on the 1:1 line, apart from the N8 surface, for which the mold slightly overpredicted the surface roughness. The measured R_z values for the molds follow a linear 1:1 relationship with surface roughness of the standards, however, they are systematically shifted; the measured mold R_z values are slightly higher than the measured R_z values of the standard.

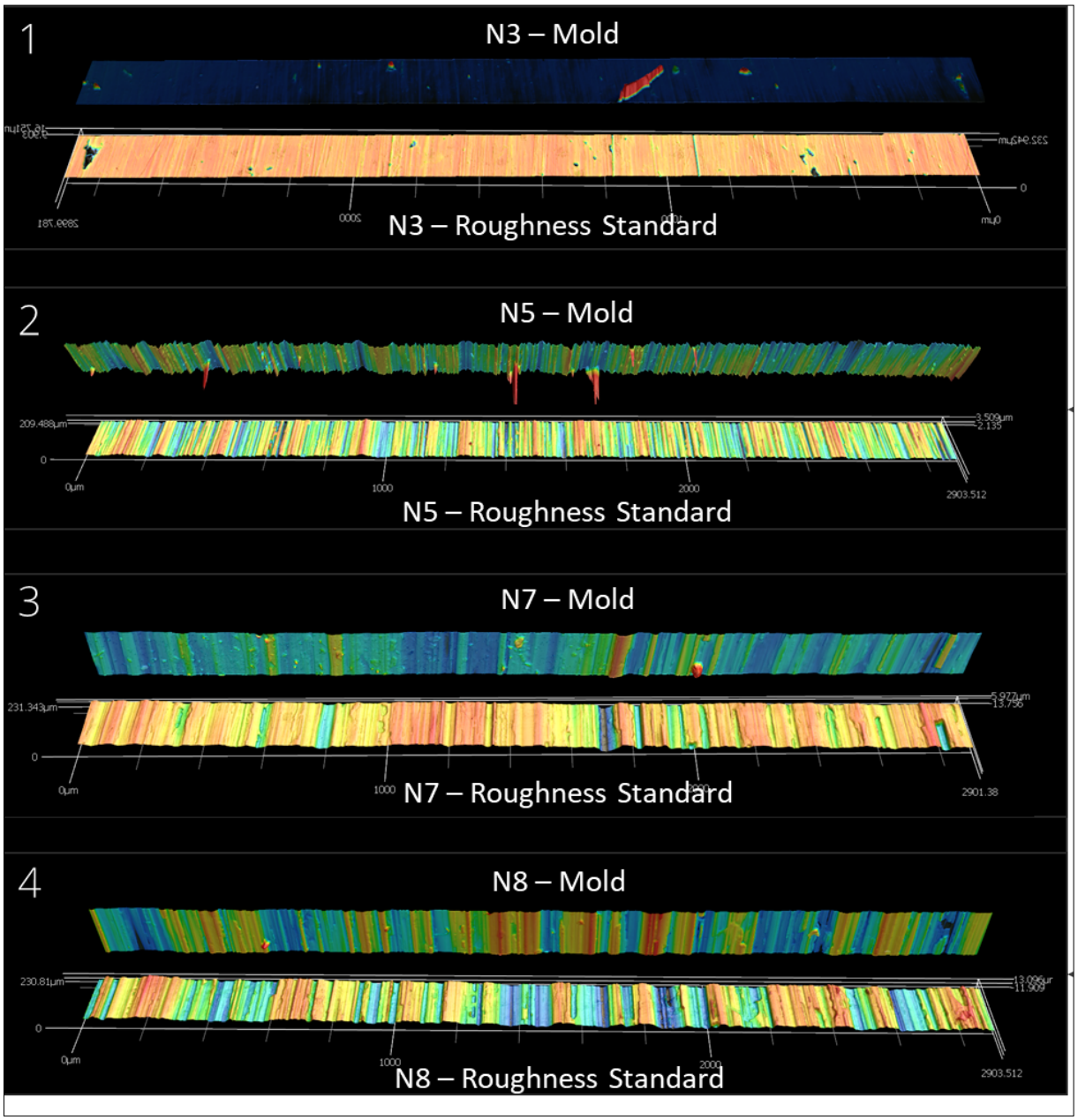

Figure 6. 3-D topographic maps of the surface roughness standards and the corresponding molds.

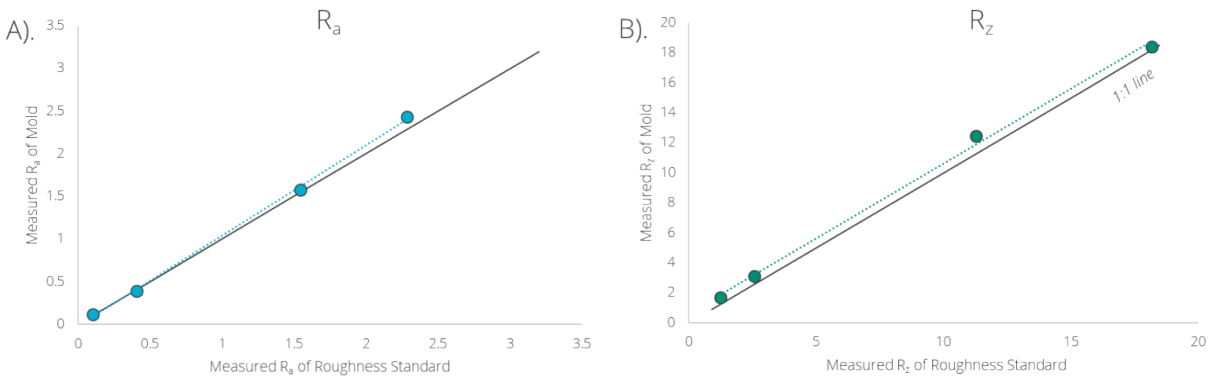

Figure 7. Measured surface roughness for the mold samples versus the measured surface roughness standard shown with a 1:1 line for a) R_a and b) R_z

2.3 Canister Sample Collection

A surface roughness survey was conducted on one of the three SNF canisters used for the CDFD project by using the surface replicating molds described previously (Section 2.1.2) [2]. The canister surveyed was 32PTH2-S023-C-H-001. Only one canister was surveyed as a representative sample, and it is assumed that the variations seen on one of the canisters adequately capture the surface features seen on the other two canisters. Canister locations were chosen to represent the range of surface features present on the canister, specifically aimed at capturing the representative "mill finish" canister surface, ground weld regions and the adjacent heat affected zones (HAZ), and any other regions that showed evidence of grinding or alteration during manufacturing. For this discussion, the HAZ region refers to the unground area adjacent to the ground weld. When the welds were manufactured, they were ground flush to the surface. There is not clear toe of the weld and therefore the boundary between the weld and the HAZ is not distinct. However, the likely width of the HAZ is 1-2 cm (as per the Sandia mock-up stress analysis [7]), so some amount of the HAZ extends outside of the relatively narrow ground area. A few examples of the altered regions that were investigated include i) large bands (~6 inches to 1 foot wide) extending several feet circumferentially around the canister, ii) specific areas (a few square inches) that have been touched up by grinding, and iii) circumferential regions near the top and bottom of the canister that have undergone additional alterations. The circumferential weld at the bottom of the canister is associated with the Inner Bottom Cover Plate, and the circumferential feature near the top of the canister is the HAZ region associated with the inner weld to mount the Support Ring as per the Final Safety Analysis Report (FSAR) [8]. Examples of these surface features are demonstrated in Figure 8. The sample locations are shown in Table 1 along with the measured R_a and R_z values of the surface replicating mold.

Surface locations were marked and the coordinates were determined using the same methodology as the photometric mapping and linked to the midpoint of the sample cell [3]. The canister is in a horizontal configuration and radially aligned by a drain hole in the grappling ring at the bottom, when the drain hole is aligned vertically (top and bottom), the canister is in its correct orientation (Figure 9). In this orientation, the longitudinal welds are at about the 4 o'clock and 10 o'clock positions (when looking at the grappling ring). The orientation of the coordinate system is shown in Figure 8a in red, where the longitudinal origin is at the open end (top) of the canister and increases toward the bottom of the canister and the axial origin is the center of the underside and increases counterclockwise. The sample coordinates are presented in Table 1 as (*longitudinal, axial*) in inches. Correlating the sampled location with the photometric map allows evaluation of the surface on a macro and micro-level to assess a wide range of surface features.

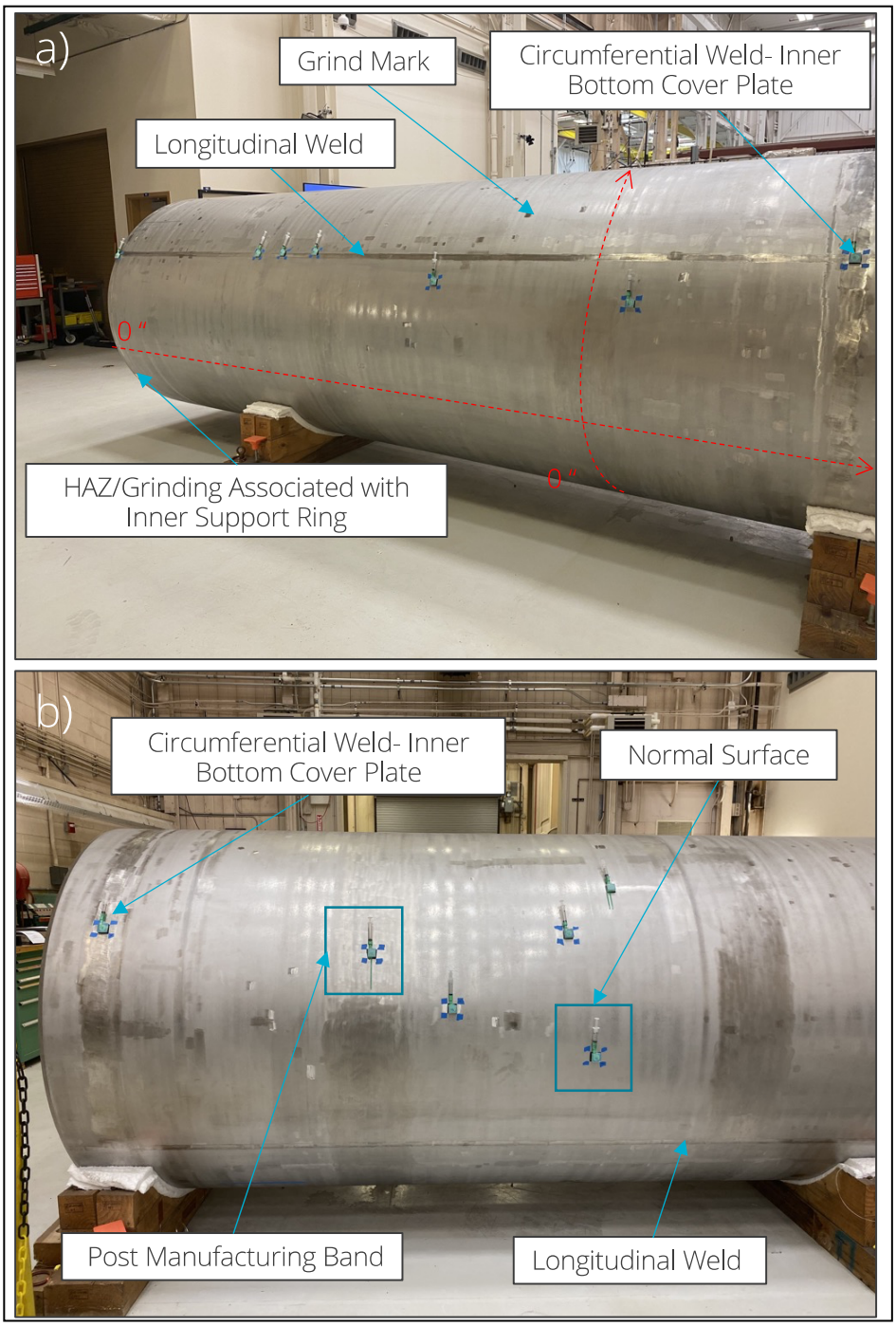

Figure 8. Photos of the canister surface with the surface sampling molds attached and various regions of interest; where a) shows an example of a Grind Mark, the longitudinal weld, the circumferential weld (Inner Bottom Cover Plate), and the HAZ/Grinding associated with the circumferential weld of the Inner Support Ring [8]. It also shows the origins in the longitudinal and axial positions used to index the sample locations for the photometric map [3]; b) shows the other side of the canister to point out the longitudinal weld, the circumferential weld (Inner Bottom Cover Plate), as well as normal surface regions and the post manufacturing bands [8].

Table 1. Sample number, canister feature, approximate canister location, measured surface roughness (R_a and R_z), and scan direction for each surface mold collected from the canister.

Sample #	Canister Feature	Approx. Coordinates[1] (inches)	R_a (µm)	R_z (µm)	Scan Direction
1	Normal Surface	(130.875, 154.875)	0.78	4.27	Vertical
2	Normal Surface	(59.625, 146.500)	0.78	4.33	Vertical
3	Normal Surface	(20.250, 146.250)	0.84	4.40	Vertical
4	Normal Surface	(115.250, 166.000)	0.84	4.51	Horizontal
5	Normal Surface	(118.375, 67.500)	0.76	3.88	Horizontal
6	Normal Surface	(158.875, 64.875)	0.75	3.75	Vertical
7	Circumferential Weld (Inner Bottom Cover Plate)	(190.250, 146.250)	0.52	2.65	Vertical
8	Circumferential Weld (Inner Bottom Cover Plate)	(190.125, 73.125)	0.53	3.00	Vertical
9-Weld	Longitudinal Weld	(82.625, 73.750)	1.41	1.86	Vertical
9-HAZ	HAZ	(82.625, 73.750)	3.19	3.33	Vertical
10-Weld	Longitudinal Weld	(71.375, 73.500)	1.05	1.54	Vertical
10-HAZ	HAZ	(71.375, 73.500)	3.02	3.15	Vertical
11	Longitudinal Weld	(73.250, 73.250)	0.81	1.58	Vertical
12	Post Manufacturing Band	(111.000, 138.750)	0.53	2.54	Vertical
13	HAZ/Grinding Associated with Support Ring Inner Circumferential Weld	(1.500, 72.250)	1.30	2.34	Vertical
14	Grind Mark	(149.750, 150.250)	0.80	2.36	Vertical
15	Grind Mark	(137.375, 158.750)	1.08	3.43	Vertical
16	Canister bottom – Grind Mark[2]	(240.625, 48.50)	0.61	3.14	Horizontal
17	Canister bottom[2,3]	(180.750, -156.625)	2.66	11.34	Horizontal

[1]The coordinates are reported (longitudinal, axial) in inches, where the open end of the canister represents 0 inches longitudinally and increase toward the bottom of the canister. To determine the axial position, the center of the canister underside represents 0 inches radially and increases counterclockwise. The locations were determined by approximating the midpoint of the sample cell on the canister.

[2] The axial position on the canister bottom is split down the middle where the underside 0 point to the top counterclockwise are positive values, and underside 0 point to the top clockwise are negative values (Figure 9).

[3] λ_c filter was not applied

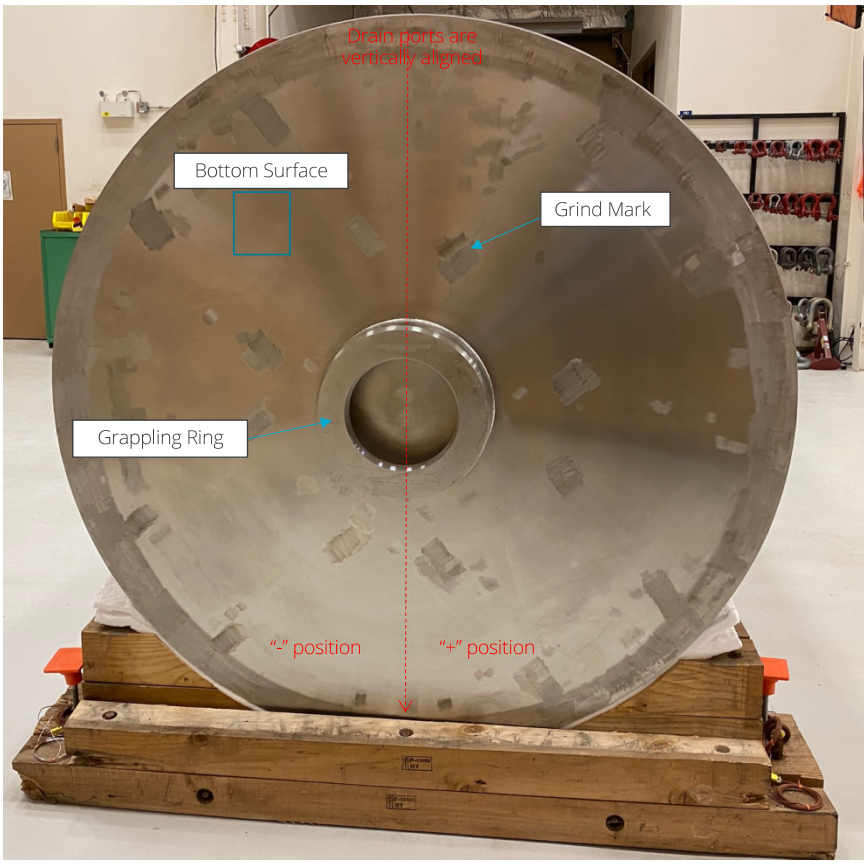

Figure 9. Photo of the bottom of the canister showing the grappling ring, bottom surface, and grind marks. In additional this image shows the orientation on how the drain ports are aligned and the coordinate system is specifically used to denote the bottom of the canister.

The surface sampling method for the canister was the same method used for the surface roughness standards. At each sampling location, the sample cell was stuck to the surface via a double-sided adhesive gasket. Then the 2-part Plat-Sil73-25 was added to the sample cell and cured affixed to the canister for ~24 hours. Once cured, the sample cells and molds were peeled off the surface and analyzed by laser profilometry, as described in Section 2.1.3, to generate negative replica of the surface of the canister.

2.3.1 Normal Surface Roughness

Six locations on the canister were chosen to evaluate the mill finish and to evaluate the variability of surface roughness across the canister. The locations were chosen to avoid any abnormal surface features. Figure 10 shows the canister locations via a photometric map [3], image of the mold in-situ and optical image, and the 3-D profile of the surface.

From the images in Figure 10 and the surface roughness values from Table 1 for Samples 1-6, it is clear that the mill finish across the canister is relatively uniform, where the average $R_a = 0.79 \pm 0.04$ µm and $R_z = 4.19 \pm 0.3$ µm. There does not appear to be any directionality, as horizontal and vertical line scans resulted in similar surface roughness values. This surface roughness corresponds to about a 180-grit surface ($R_a = 0.76$ µm [9]).

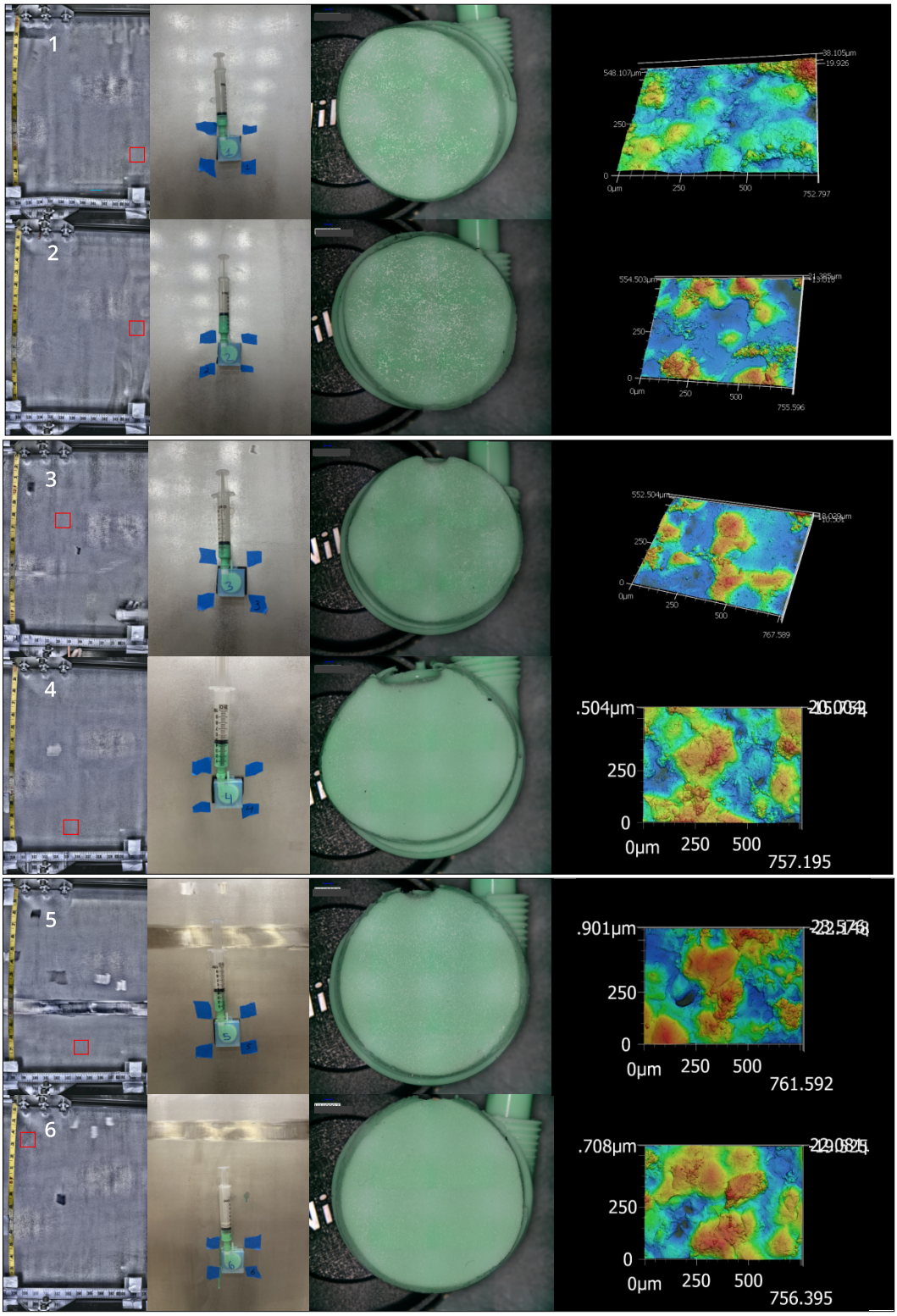

Figure 10. Samples 1 - 6 showing the photometric mapped location (red square) [3], the mounted surface mold, optical image of the surface mold, and a 3-D topographic map of the surface obtained by laser profilometry analysis demonstrating normal canister roughness.

2.3.2 Post Manufacturing Band

Apart from the normal surface, that next most common surface features were large circumferential bands that occurred periodically, as seen in Figure 8. These large bands were about ~6 inches to 1 foot wide in the longitudinal direction and spanned several feet to most of the of the canister circumferentially. These regions were visually distinct from the normal surface and possibly attributed to direct contact with the rollers when the canister was manufactured. One sample (Sample 12) was collected from one of these bands to evaluate the deviation in the surface roughness compared to the normal canister roughness. The sample results are shown in Figure 11 and Table 1.

The surface roughness of this band from the 3-D topographic map looks similar to the normal roughness samples, however the R_a and R_z values of this surface feature were less than the normal surface – thus representing a smoother surface. The R_a value was determined to be 0.53 ± 0.01 µm and the R_z was determined to be 2.54 ± 0.4 µm. There was no clear directionality of the surface features, which just appear to be a muted version of the normal surface, suggesting that this is a result of the rollers in contact with the SS during manufacturing. Based on the measured R_a value, this surface is slightly rougher than a 220-grit finish.

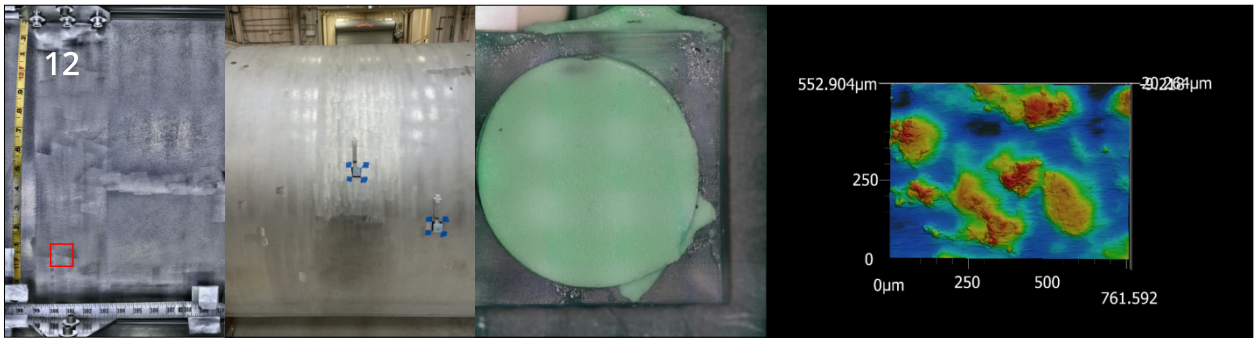

Figure 11. Sample 12 showing the photometric mapped location (red square) [3], the mounted surface mold, optical image of the surface mold, and a 3-D topographic map of the surface obtained by laser profilometry analysis of the surface roughness of the Post Manufacturing Band.

2.3.3 Welds and HAZ Regions

Welds and HAZ regions are of great interest as these regions are likely to contain high weld-related tensile stresses and hence, are likely to be the most susceptible locations for CISCC. On this canister there are two longitudinal welds that are 180° apart and span the entire length of the canister, which are visible in Figure 8. Associated with these longitudinal welds are HAZ regions that extend several cm beyond the weld on either side. In addition to the longitudinal weld, there were also two circumferential features associated with welds at the top and bottom of the canister. The one at the top of the canister is the external HAZ associated with the internal weld used to mount the Inner Support Ring and was about the same width as the longitudinal weld. The circumferential weld at the bottom of the canister was 2-3 in wider than the longitudinal weld and visually appeared to have much more surface variation than the weld. This weld was associated with welding the Inner Bottom Cover Plate and there are several designs of this feature shown in the FSAR, the one on this canister likely consists of multiple welds [8].

2.3.3.1 Longitudinal Weld and Associated HAZ

The samples collected from the longitudinal welds were Samples 9, 10, and 11; Samples 9 and 10 were bisected by the weld and therefore also included the unground HAZ regions (Figure 12). The differences between the weld region and the HAZ region can be observed visually on the surface mold and in the 3-D maps. From the 3-D topographic maps of the welded regions, they appeared to have some directionality to them, where the fine surface features were parallel to the weld direction. This reflects the fact that the weld beads were ground away after welding. The profilometry scan direction was collected in the vertical orientation to account for this directionality. 3-D topographic maps collected from the HAZ regions resemble the mill finish, and do not appear to have any clear directionality.

The average surface roughness values for the weld regions were $R_a = 1.09 \pm 0.3$ µm and $R_z = 1.66 \pm 0.2$ µm. These regions had a higher R_a value than the normal surface but a lower R_z value. This suggests the roughness of the weld in terms of surface variability is greater than the normal surface, consistent with the visible grind marks; however the depth of the features observed is generally smaller. The variation was much more substantial than seen for the normal surface. Samples 9, 10, and 11 were actually placed very close to each other in the longitudinal direction along the weld. However, Sample 9 had an $R_a = 1.41$ µm and Sample 11 had an $R_a = 0.81$ µm. The weld regions on average corresponded with a grit of ~ 150, however the corresponding grits for this large R_a range for the welds ranged from about 120-grit to 180-grit.

The associated images of the HAZ regions, which are the unground regions adjacent to the welds, were evaluated by analyzing the top section of Samples 9 and 10, are shown in Figure 12. There was no clear directionality of the HAZ region, and topographically, the HAZ regions resemble the normal surface, and have a similar R_z value, though the R_a value is very different. The average HAZ $R_a = 3.11 \pm 0.2$ µm and the $R_z = 3.24 \pm 0.1$ µm. This suggests that the overall surface of the HAZ regions is rougher than the normal surface, but the difference between the peaks and valleys is quite similar and even slightly less. Due to the large R_a, the HAZ regions resemble a surface finish of 60 – 80 grit.

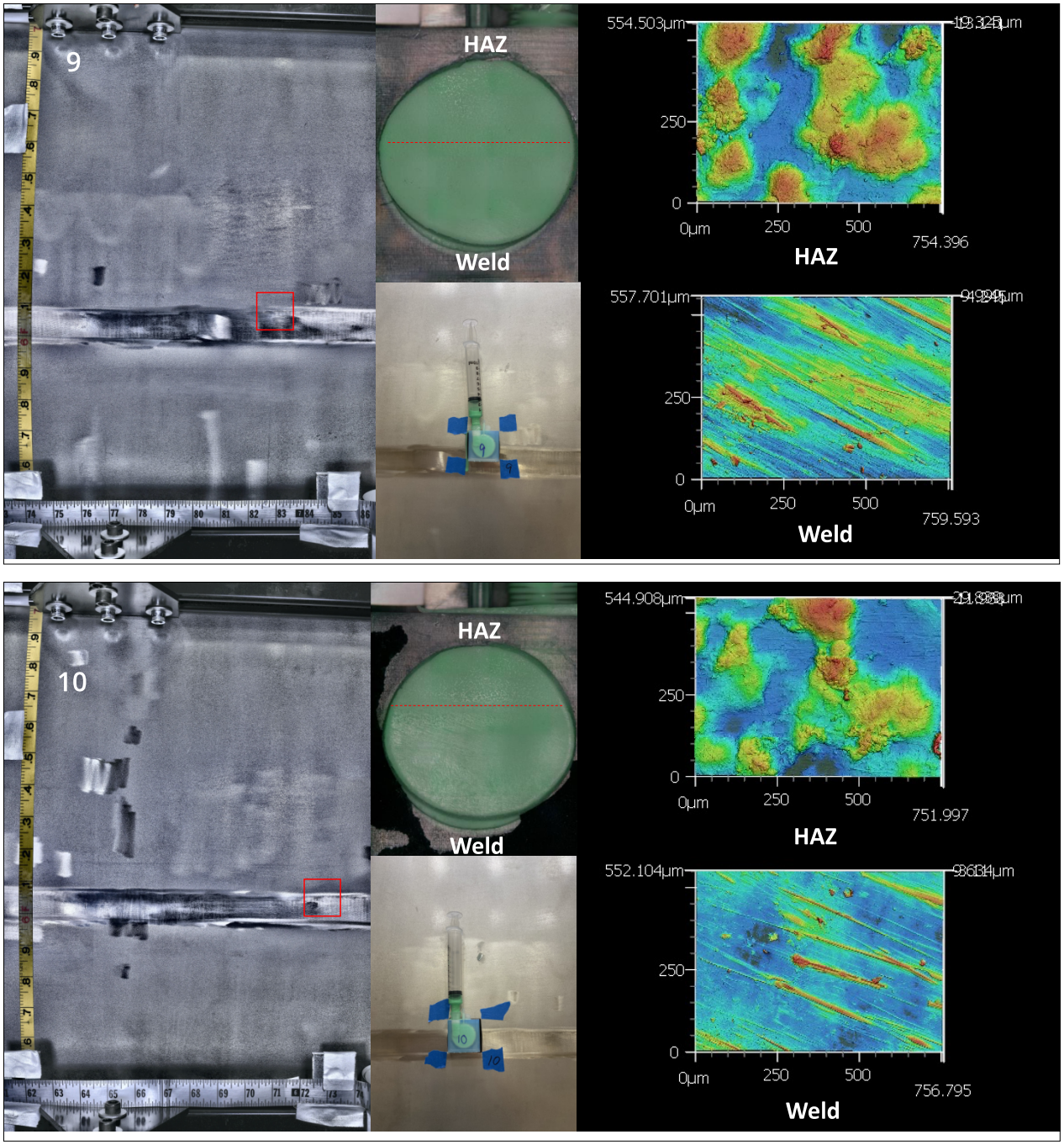

Figure 12. Samples 9 and 10 showing the photometric mapped location (red square) [3], the mounted surface mold, optical image of the surface mold, and a 3-D topographic map of the surface obtained by laser profilometry analysis of the surface roughness of the longitudinal weld and HAZ region.

2.3.3.2 HAZ/Grinding Associated with the Support Ring Circumferential Weld

Sample 13 was collected at the intersection of the longitudinal weld and the external HAZ region resulting from the circumferential weld used to mount the Internal Support Ring at the top of the canister (Figure 13). The external surface of this surface appears to have been ground spanning the entire circumference. In addition, a few small mechanically-formed pits were visually observed and evaluated by profilometry (see Section 2.3.4.1.).

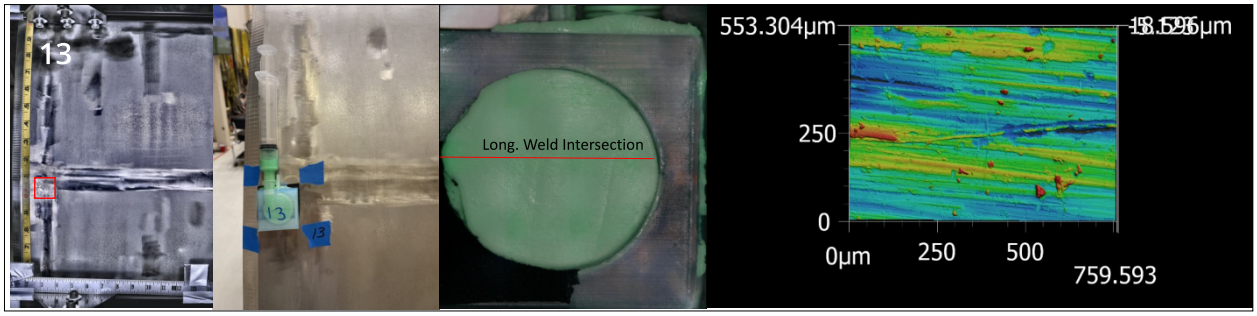

Figure 13. Sample 13 showing the photometric mapped location (red square) [3], the mounted surface mold, optical image of the surface mold, and a 3-D topographic map of the surface obtained by laser profilometry analysis of the surface roughness of the intersection of the longitudinal weld and HAZ/grind region associated with the Support Ring inner circumferential weld.

The topographic map of Sample 13 resembled the longitudinal weld. It contained the directionality in parallel to the weld direction. The measured R_a was 1.30 ± 0.2 µm and R_z was 2.33 ± 0.5 µm. This surface roughness was very similar to Sample 9, which was the roughest of the longitudinal weld samples and corresponded to a surface roughness of about 120-grit. This region was not as rough as the HAZ associated with the longitudinal welds; however, the R_a was much higher than other regions that had been ground.

2.3.3.3 Circumferential Weld Associated with the Bottom Cover Plate

Samples 7 and 8 were collected from the circumferential weld at the bottom of the canister associated with the Inner Bottom Cover Plate (Figure 14). Like the longitudinal welds, the circumferential welds had been ground to remove the surface weld beads. In contrast to circumferential feature represented by Sample 13, the surface features observed in the bottom circumferential weld were visibly larger and smoother when looking at the canister surface. The surface roughness of Samples 7 and 8 more closely resembled the large, post-manufacturing band, but had the directionality of the welded regions. The measured roughness of this canister feature was R_a = 0.52 ± 0.01 µm and R_z = 2.82 ± 0.2 µm corresponding to a 220-grit surface finish. Relative to the longitudinal welds, there is much less variability in the R_a and R_z values as well as smaller R_a values overall.

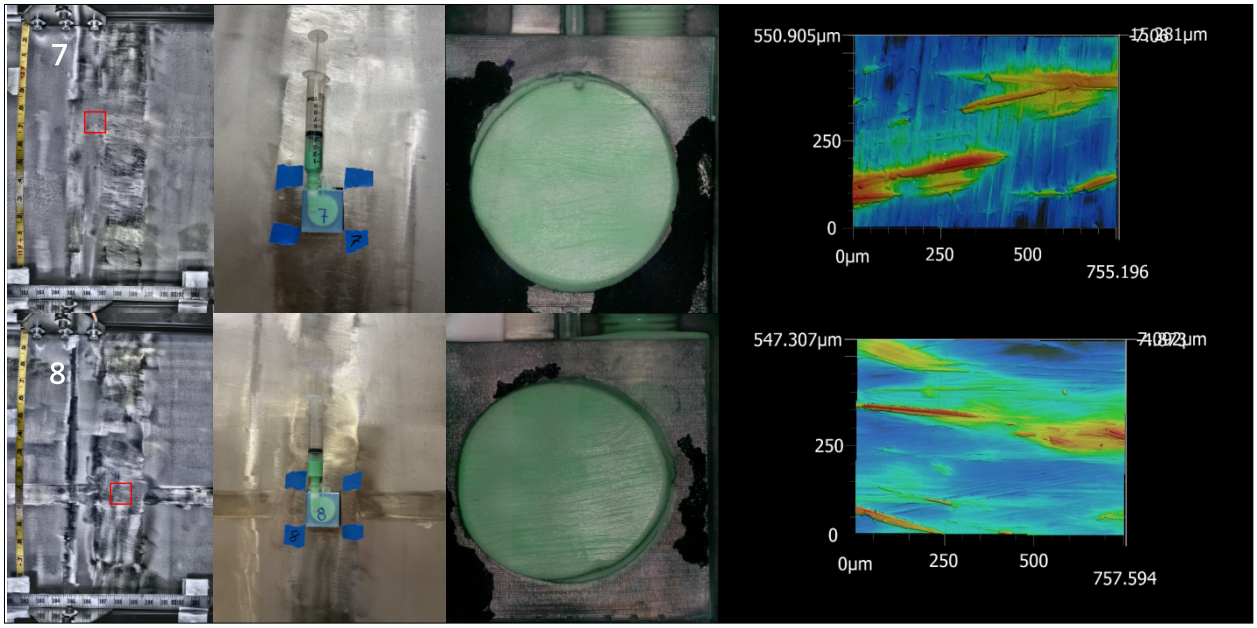

Figure 14. Samples 7 and 8 showing the photometric mapped location (red square) [3], the mounted surface mold, optical image of the surface mold, and a 3-D topographic map of the surface obtained by laser profilometry analysis of the surface roughness at the circumferential weld associated with the Inner Bottom Cover Plate.

2.3.4 Grind Marks

Scattered across the canister were small regions that had been ground. It is unclear why these regions were ground, however there are many of them across the canister surface. These grind regions may have been performed post manufacturing to remove specific flaws. Two locations were chosen to evaluate the surface roughness of these ground regions. Both regions had visible mechanical pits in the processed region. The mechanically induced pits in these samples were evaluated further in Section 2.3.4.1.

The grind marks were visually distinct features on the canister. The 3-D topographic maps of the surface resemble other features that have been further altered beyond the normal surface topography (Figure 15). There is clear directionality in the orientation of the surface features that align parallel to the canister direction, similar to the welds. The average R_a was 0.94 ± 0.2 µm and R_z was 2.90 ± 0.76 µm. There was a decent amount of variability between the two samples and the roughness spanned comparable grinding roughness of 150-180 grit.

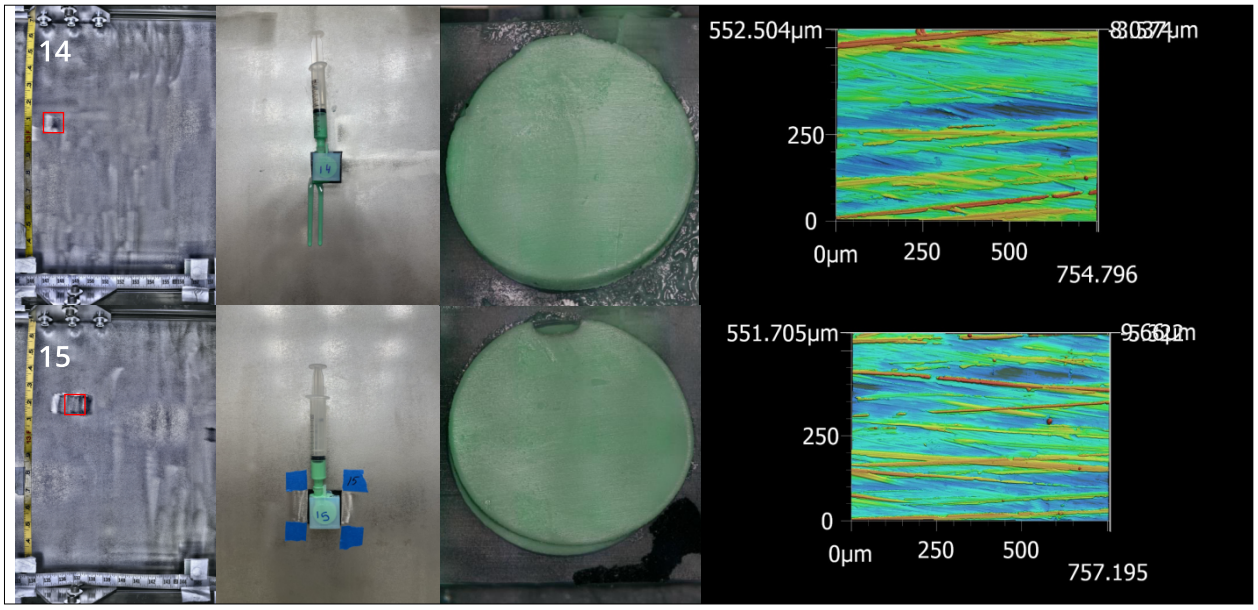

Figure 15. Samples 14 and 15 showing the photometric mapped location (red square) [3], the mounted surface mold, optical image of the surface mold, and a 3-D topographic map of the surface obtained by laser profilometry analysis of the surface roughness of grind marks.

2.3.4.1 Mechanically Formed Pits

Mehcanically formed pits were observed on the canister surface co-located with three of the samples (Sample 13, 14 and 15). These pits did not form by corrosion but rather are due to some mechanical process or formed during the manufacturing. In total, 20 pits were identified and analysis via profilometry of these pits was performed to assess their size and aspect ratio. The pits were generally hemispherical or semi-hemispherical with significant variability in the pit depth and width. The pits were generally pretty shallow, as the average pit depth was 31.63 ± 19.8 µm, and the deepest measured pit was 85.67 µm from Sample 14. The pit width was generally much larger than the depth and often more than hundreds of microns wide, ranging from 48.15 µm (Sample 14) to 1878 µm (Sample 15). Figure 16a shows the distribution of pit width and depth of all the measured pits associated with Samples 13, 14, and 15. The average aspect ratio was calculated (excluding the two outliers from Sample 14 with an aspect ratio near 1) as [Pit Depth/Pit Width] and was plotted on the pit width versus pit depth graph. Overall, the average aspect ratio of the pits was 0.04 ± 0.02, which represents a very shallow wide pit and are likely not significantly more suspectable to CISCC than the bulk of the surface. The cumulative probability plot of the aspect ratio (Figure 16b) shows that the majority of the pits > 90 % had an aspect ratio < 0.1.

There were a few notable exceptions in pit geometry. Of the identified pits, there were a few pits associated with Sample 14 that either had a higher aspect ratio or features that resembled microcracks. Two of these pits are shown in Figure 17. In Figure 17a, a small microcrack-like feature or fissure can be seen near the top of the hemispherical pit (near the yellow line) and Figure 17b, shows examples of two small pits with an aspect ratio ~ 1. These are notable for two reasons, 1) if a brine is present, these can act as crevice formers, thus creating occluded cells that can accelerate corrosion, and 2) as the aspect ratio increases, these features, in the presence of a stress field, can act to concentrate it, thus leading to more susceptible locations for CISCC initiation [10-14].

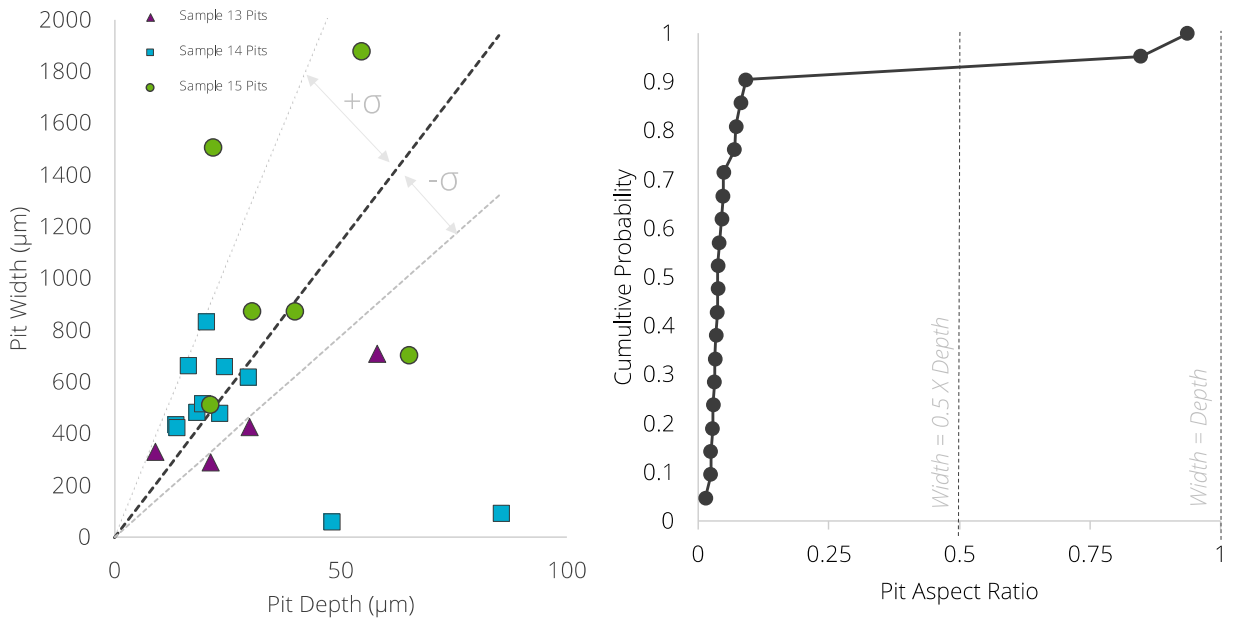

Figure 16. a) The pit width versus pit depth shown with the average and standard deviation of the pit aspect ratio (excluding the two outliers with a high aspect ratio) shown with the standard deviation (σ), and b) Cumulative probability versus aspect ratio of the mechanical pits identified.

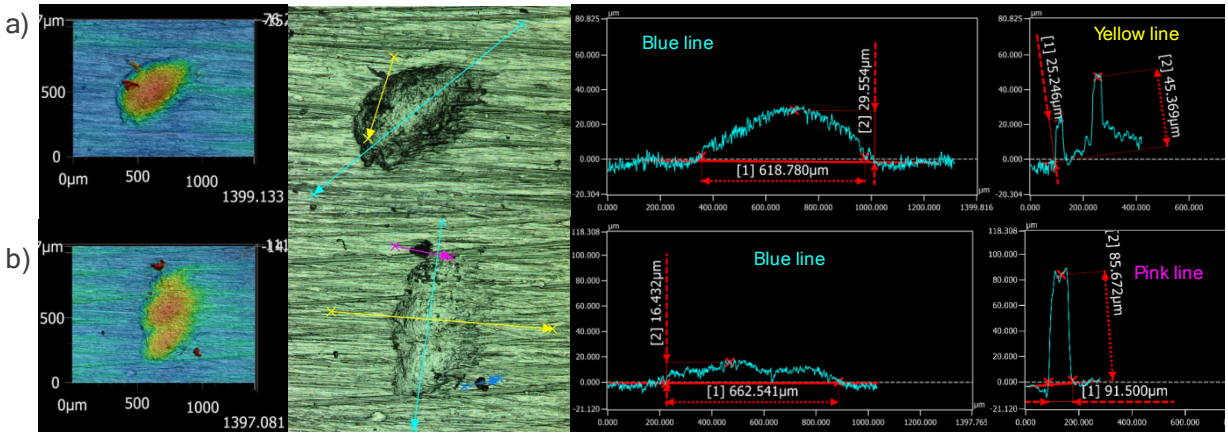

Figure 17. Pit analysis of two pits from Sample 14. The main pit in both cases is semi-hemispherical shallow and wide. a) Displays a small crack-like feature extending out from the rim of the pit, and b) has two narrow and deep pits adjacent to the main pit, these two pits have an aspect ratio ~1.

2.3.5 Canister Bottom Near the Grappling Ring

The final two samples were collected from the bottom of the canister. The bottom of the canister is distinctly different from the rest of the canister surface as it has obvious fine, uniform grooves. Like the normal surface, the bottom of the canister had several randomly distributed grind marks. One sample, Sample 17, was collected to be representative of the bottom surface, and Sample 16 was a grind mark on the bottom surface of the canister. During the CDFD campaign, no dust analysis samples will be collected from the bottom of the canister, but the roughness was evaluated to understand the variation of surface features across the entire canister.

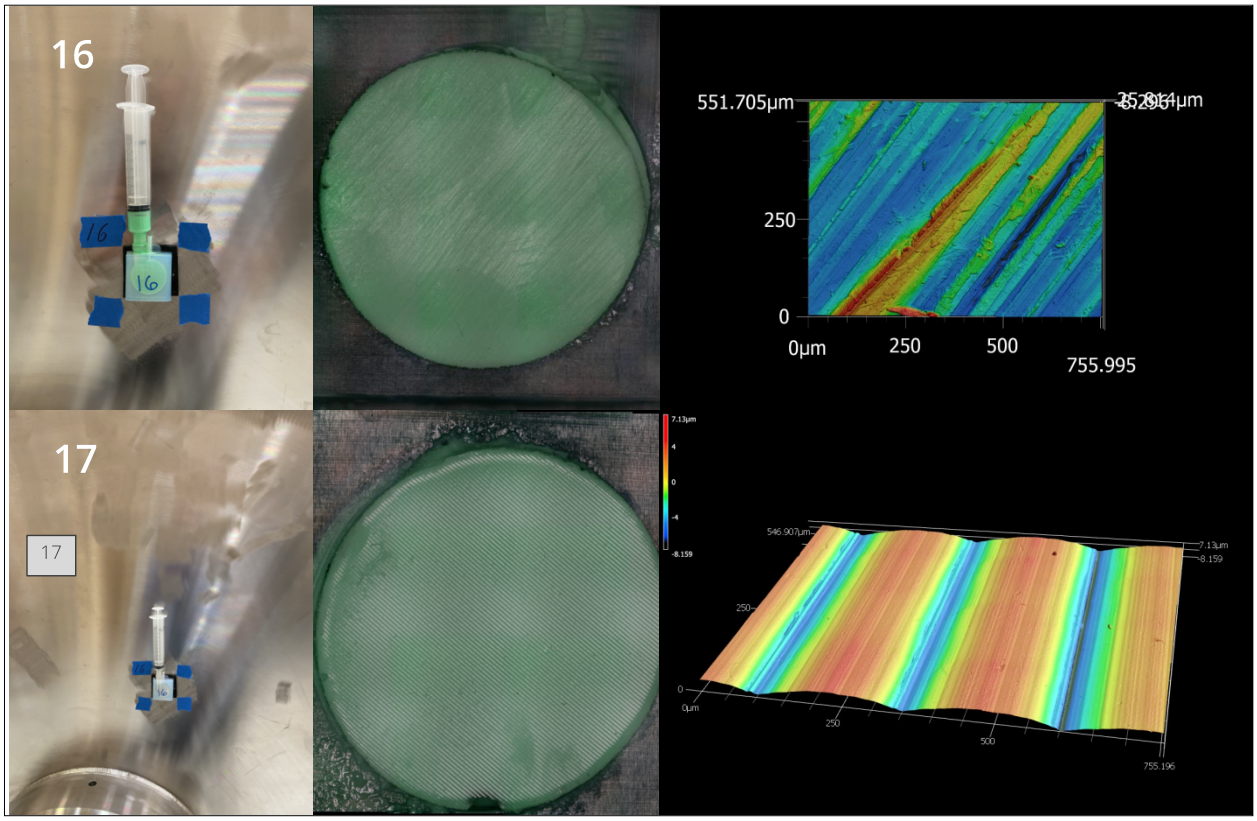

Figure 18. Samples 16 and 17 showing the mounted surface mold, optical image of the surface mold, and a 3-D topographic map of the surface obtained by laser profilometry analysis of the surface roughness of features on the bottom of the canister. Sample 17 is a representative sample from the bottom, while Sample 16 has been further machined.

The normal surface topography (Sample 17) at the bottom of the canister is very uniform with small surficial grooves that run parallel to larger grooves at a uniform interval, about every 250 µm (Figure 18). The reported R_a and R_z values did not use a Λ_c filter because the filter removed the long-range features of the surface. The overall surface was much rougher than the normal surface roughness with R_a = 2.66 µm and R_z = 11.34 µm and corresponds to a < 80-grit surface.

Although the bottom of the canister is distinct from the bulk of the canister, the grind mark (Sample 16) on the bottom of the canister resembles the grind marks found across the canister. The primary difference is that the orientation runs radially along the grooved surface. The measured surface roughness was R_a = 0.61 µm and R_z = 3.14 µm, corresponding to ~180 – 220-grit surface.

2.4 Impact of the Surface Roughness Measurements

The microscale surface roughness features are important to evaluate as they may play a role in dust deposition and accumulation. Surface roughness has also been shown to be an important variable with respect to corrosion [15, 16]. Current dust deposition models do not account for surface roughness and the impact that may play on dust deposition. One reason for this omission is that variations of the surface roughness on the canister had not been known. Through the survey conducted on 32PTH2-S023-C-H-001 we have developed a reasonable understanding of the surface roughness and any significant deviations associated with specific surface features. Figure 19 presents a summary of the measured R_z versus R_a values for each canister feature and are shown with a corresponding grit size (based upon R_a).

This figure displays that the majority of the canister has very similar surface roughness, where the normal surface, circumferential weld associated regions, and post manufacturing bands have similar R_a, R_z, and (R_a/R_z) values (Figure 20). Deviations in surface roughness were found in areas associated with the welds, HAZ, and grind marks; where generally the R_z value were similar to the bulk of the surface, but the R_a tended to be greater. Another deviating feature is the directionality of the surface. The normal surface, post manufacturing bands, and HAZ regions have no distinct directionality to them, in contrast, areas that have been welded or ground have directionality that typically runs parallel to the longitudinal weld direction. During sampling campaigns for the CDFD project, when possible, the relationship between dust accumulation and surface roughness will be evaluated, specifically with respect to the weld and HAZ regions versus the normal surface.

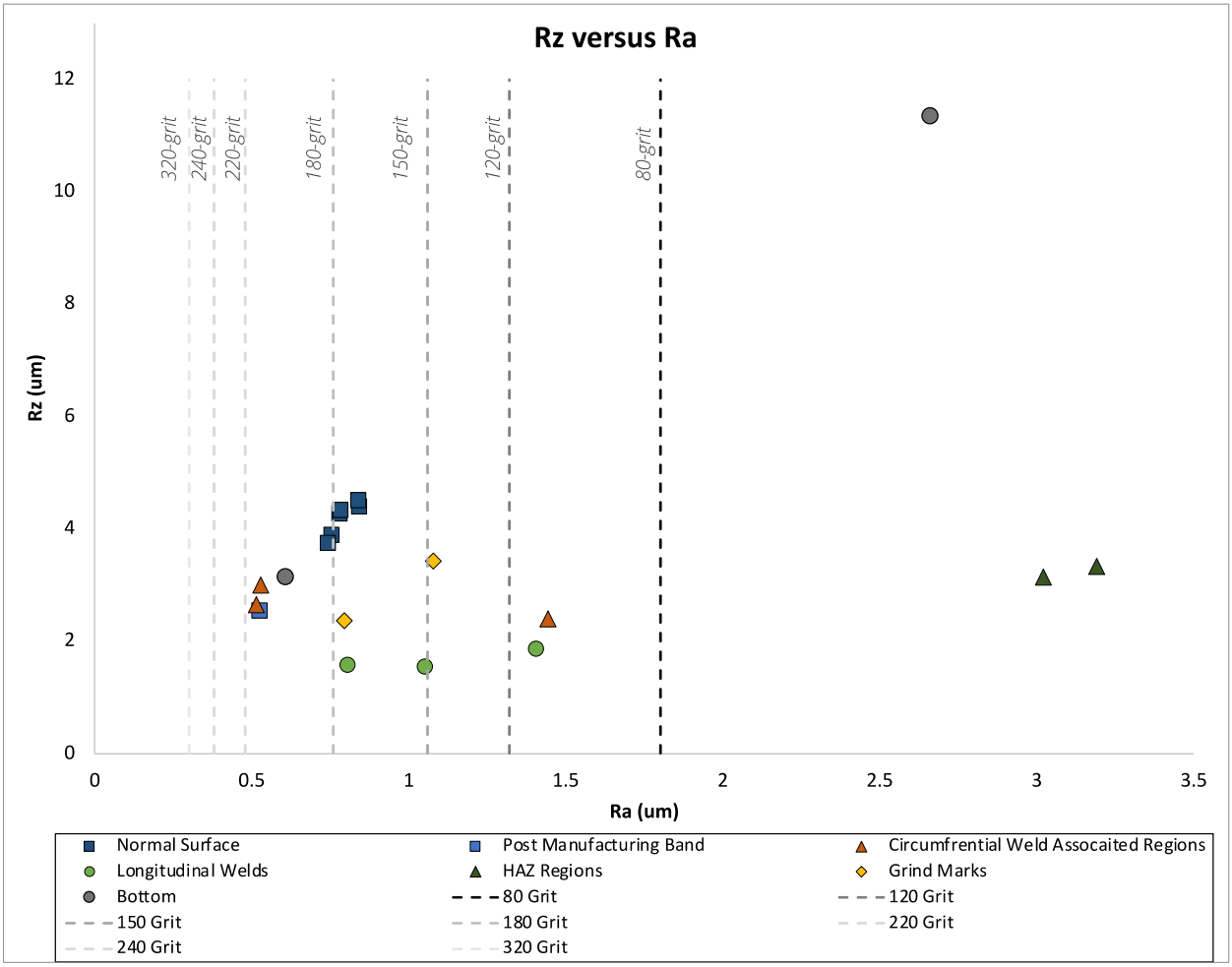

Figure 19. R_z versus R_a for each of the sampling molds representing different surface features shown with surface finishes with respect to a known grit size.

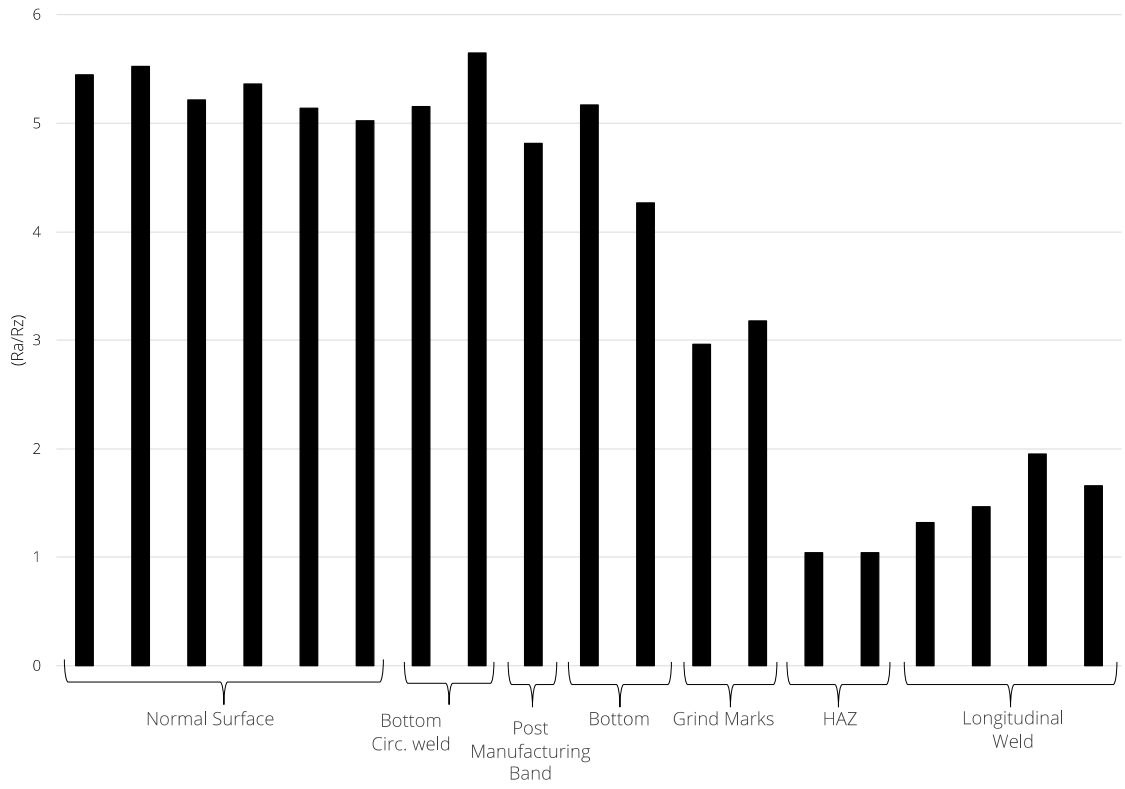

Figure 20. R_a/R_z for various surface features.

Another valuable result from these measurements is the identification of realistic surface roughness for corrosion testing. With respect to corrosion, increased surface roughness may enhance localized corrosion susceptibility [15, 16]. Residual stresses due to surface grinding may also influence pit morphology as well as microcracking [14]. Surface roughness measurements add another reason why the welds and HAZ regions are likely to be most susceptible to localized corrosion and CISCC due to the fact that these regions generally had rougher surfaces, as seen by higher R_a values and greater deviations in surface roughness.

Overall surface roughness may affect the air flow which would impact the dust deposition as well as affect the planned sampling strategy if it is determined that there exists a correlation between surface roughness and dust accumulation during early testing. As salts begin to deliquesce on the surface, salt redistribution can occur. The local surface roughness may also play a role in how the surficial brine interacts with the surface. The evaluation of the surface roughness via the analysis of surface replicating molds allows for us to estimate the variation in the surface roughness across the canister with respect to the most common surface features. These results demonstrate canister relevant surface roughness and can act as input parameter for dust deposition model, corrosion testing, and testing during the CDFD campaign.

3. EVALUATION OF SPOT WELDS, ATTACHMENT SHIMS, AND THERMOCOUPLE WIRES FOR THERMAL MEASUREMENTS AND INDEX MARKS FOR CANISTER SAMPLING LOCATIONS

The three canisters for the CDFD project will be exposed at different heat loads (high – 40 kW, medium – 10 kW, and 0 kW- ambient). As such, it will be desirable to monitor the canister surface temperatures. To do so, it will be necessary to attach thermocouples (TC) at specific locations around the canister, with TC wires running the circumference of the canisters themselves. However, it is also necessary to determine whether the wires and attachment techniques may influence or exacerbate canister surface corrosion, thus potentially disrupting dust deposition testing and/or leading to failure of the TCs over the lifetime of the CDFD exposure. Additionally, these wires and attachments (or attachment methods such as spot welding) may serve a dual purpose as markings for orientation on the canister surface dust sampling. In order to examine the aging and lifetime, and potential detrimental effects of TC wires and attachments, a mock-up plate was designed and exposed under accelerated canister relevant conditions.

3.1.1 Design and setup of mockup plate

The sample plate was designed as shown in the mock-up plate schematic and image in Figure 21. SS 316L (SS316L) sheet was procured, cut into two sheets (~ 6 x 12”), and welded. Prior to welding, each sheet was surface ground and finished. In Figure 21, the upper portion was ground to a 50-grit SiC paper while the lower portion was finished with a mill finish (shown in Figure 22). These surface finishes were selected to mimic different regions of the canister surface (i.e. unwelded regions and regions where weld beads were ground down). After finishing, the surfaces were rinsed and cleaned with ethanol to remove any excess polishing grit. The two SS316L portions were then beveled along the edge to be welded. A single V-groove butt weld was used, in which the two pieces were fused together, first without any material filler, the part was allowed to cool, the oxide was then cleaned off the surface using abrasive discs mounted to a die grinder, then a final filler pass was welded using 316L filler metal. While this is not the exact welding procedure applied to the SNF canisters (due to scale and availability of tooling), it was used to represent a canister weld region on the surface (Figure 23). After welding, the weld region and HAZ were ground down using the same 50-grit SiC paper. A matrix of materials, wires, and cutting techniques were examined to determine the best selection (least detrimental) for aging and lifetime over the CDFD exposure period. Two different materials of TC wires were tested; SS316L and Inconel (a precipitation hardened Ni-Cr alloy). These were attached with two types of shim materials; a nichrome shim and a SS shim, following the pattern laid out in Figure 21a. The shims and TC wires were cut using one of three types of scissors; 1) a Kline SS scissor, 2) a SS 410 scissor, or 3) a Medical-Pro high grade surgical SS scissor, again following the pattern in Figure 21a. The range of scissor materials were examined to determine if potential material contamination during cutting could influence material aging. A spot welder, with two different tips, tungsten or copper, was used, again following the pattern show in Figure 21a. The shims were attached with 5 spot welds on either side of the TC wire, as shown in Figure 24.

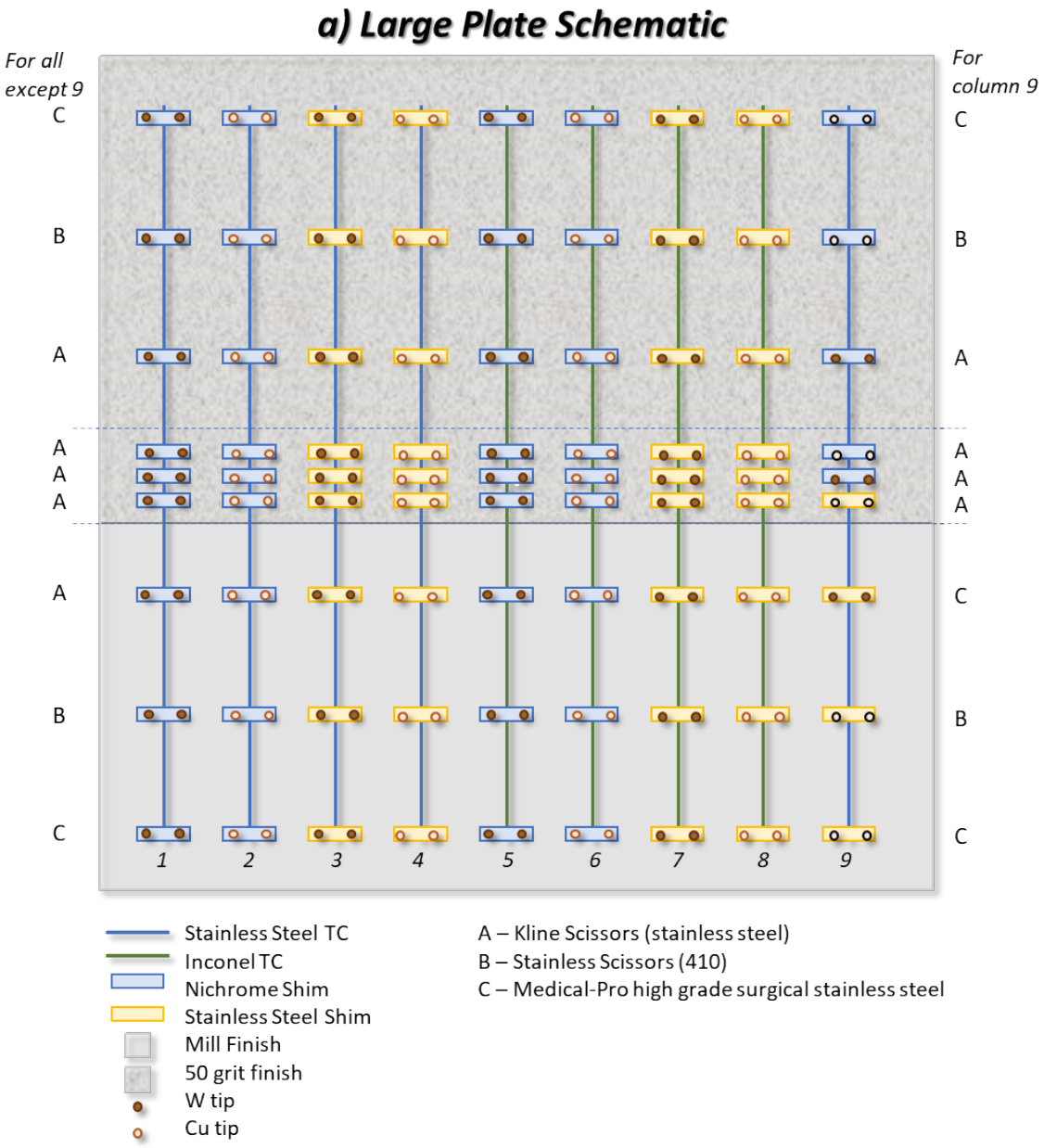
a) Large Plate Schematic
For all except 9
For column 9
C
B
A
A
A
A
A
A
C
B
C
C
B
A
A
A
C
B
C
1
2
3
4
5
6
7
8
9
Stainless Steel TC
Inconel TC
Nichrome Shim
Stainless Steel Shim
Mill Finish
50 grit finish
W tip
Cu tip
A – Kline Scissors (stainless steel)
B – Stainless Scissors (410)
C – Medical-Pro high grade surgical stainless steel

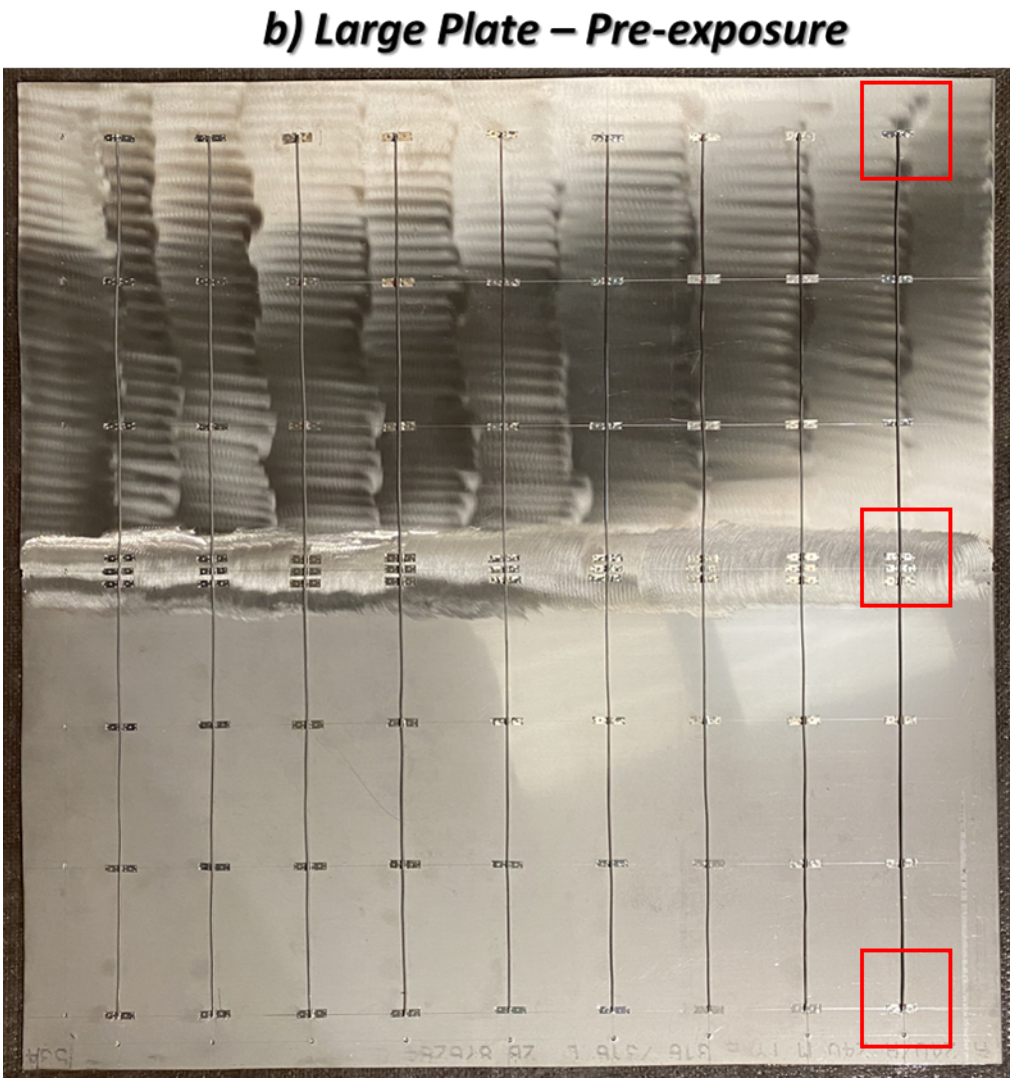

Figure 21. a) Schematic of plate mockup for spot weld, attachment shim, and thermocouple testing, and b) image of actual plate (red boxes highlight shims shown in Figure 26).

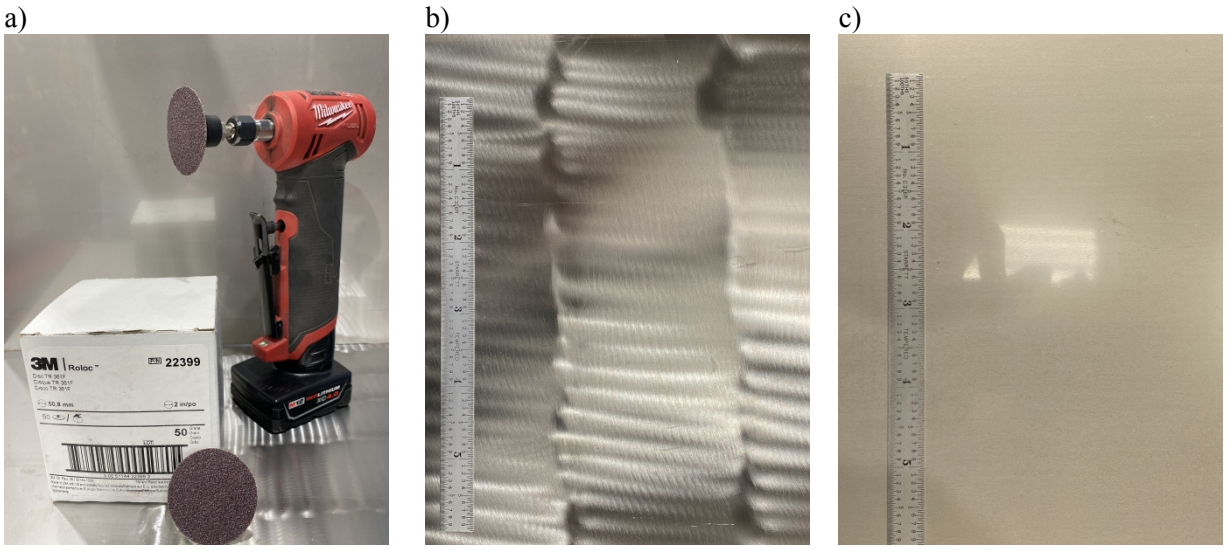

Figure 22. a) Grinding paper and tool, b) grind finish surface, and c) mill finish surface of SS316L plate. Ruler shown for scale.

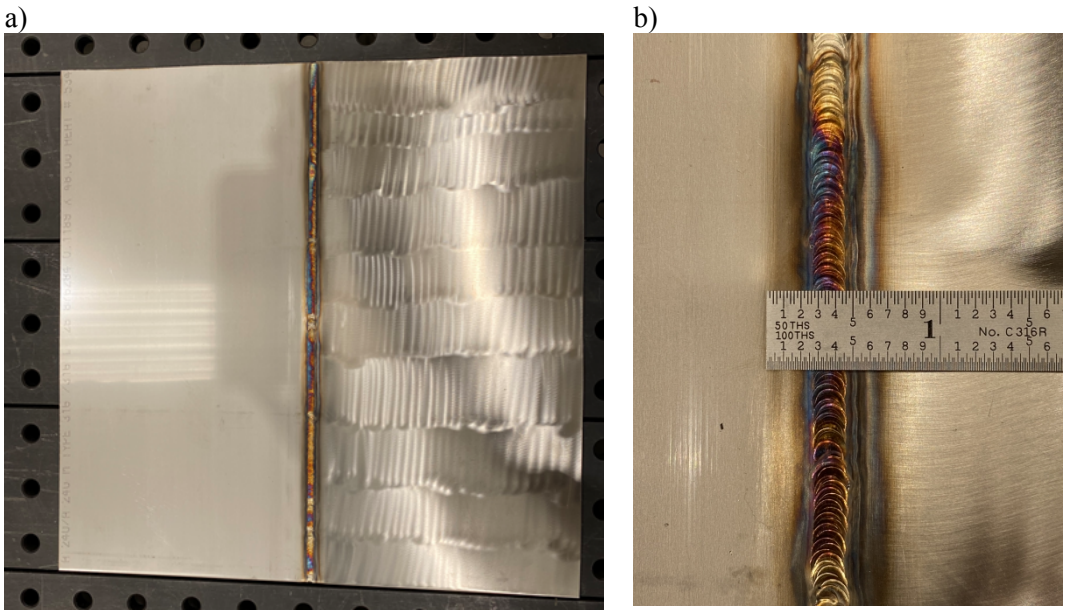

Figure 23. a) Welded mockup SS316L plate and b) inset of weld (ruler for scale).

a) b)

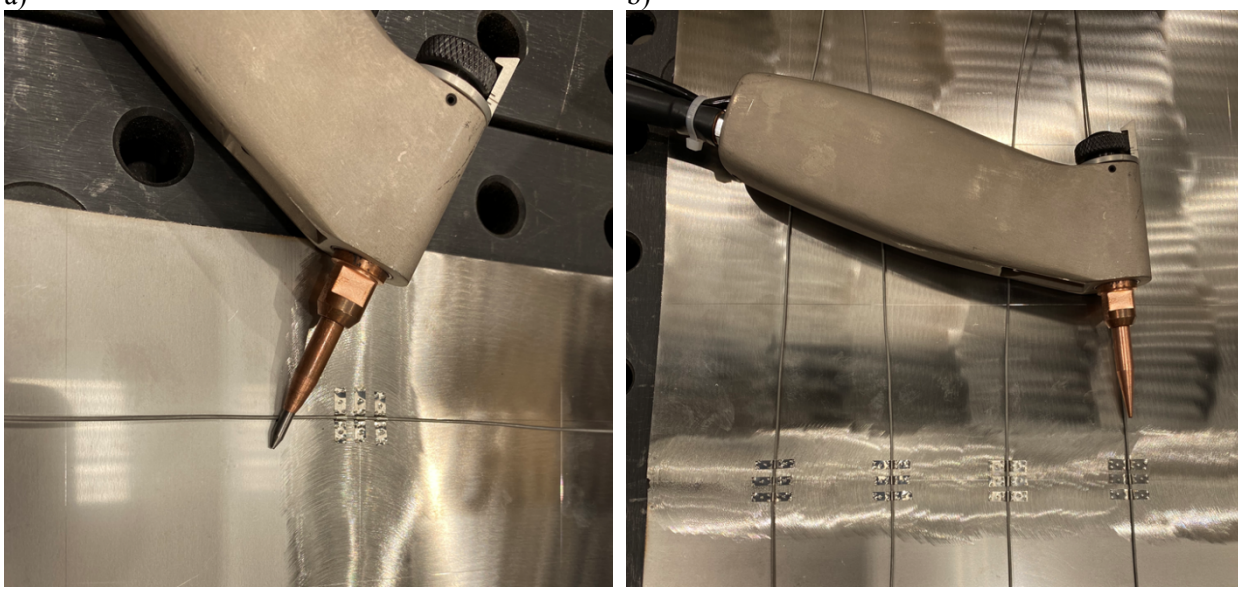

Figure 24. Spot welding with a) W tip and b) Cu tip.

3.1.2 Atmospheric testing of mockup plate

Atmospheric testing of the mockup plate was carried out in accelerated canister relevant exposure conditions. Prior to exposure, the plate was coated with 300 µg/cm^2 chloride of ASTM sea water solution using an SNL built nebulizer system. An example of the salt deposition process is shown for the plate in Figure 25a with representative salt deposition (shown on a sapphire surface) in Figure 25b. Salt particles are distributed uniformly and evenly across the surface in size ranges the replicate closely those of atmospheric sea salt aerosols (10s of µm).

a) b)

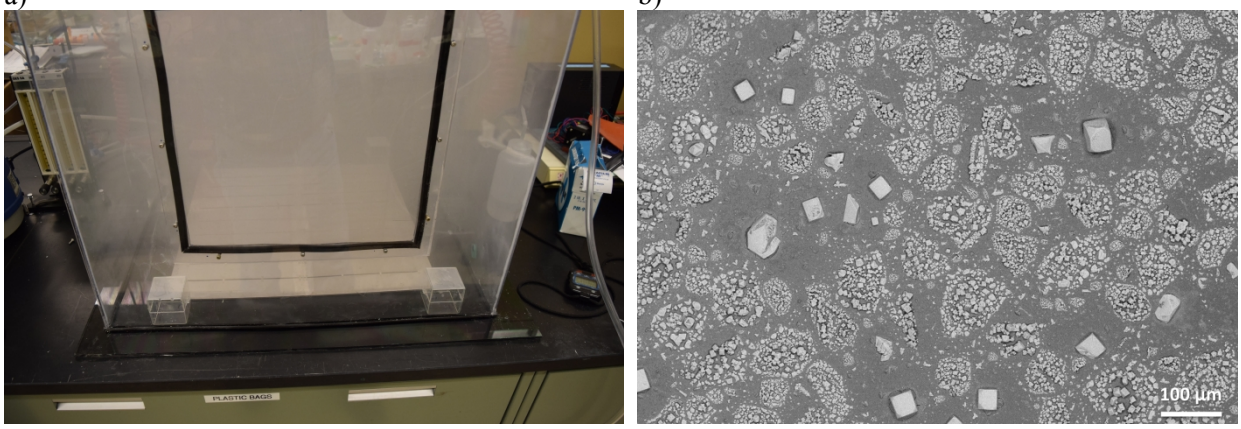

Figure 25. Salt deposition a) image of SS316L mockup plate in nebulizer chamber with salt fog and b) example SEM image of nebulized sea salt deposition.

After deposition of salt on the surface, the mock-up plate was then loaded into a temperature and humidity-controlled chamber and exposed for 3 months under cyclic conditions (cycle presented in Table 2). The development of these accelerated test conditions is described in the FY21 Year End CISCC report [2]. The plate was periodically removed (24 h, 72 h, 7 days, 14, days, 1 month, and 3 months) to

assess the potential for ongoing corrosion damage. The exposure remains ongoing, and further analysis and/or exposure plans will be described below.

Table 2. Calculated cyclic atmospheric parameters modeled after Arkansas nuclear 1 weather

Hour	Temperature, ºC	RH, %
2	41.68	30.33
4	36.45	41.68
6	35.27	43.92
8	34.35	46.69
10	33.69	48.68
12	32.74	49.54
14	33.44	49.57
16	38.24	40.98
18	40.55	34.62
20	42.69	30.62
22	43.51	27.82
24	42.97	29.15

**Note: Cyclic chamber can only be programmed out to 0.1 decimal place, thus conditions here were rounded for exposure inputs.*

3.1.3 Initial atmospheric exposure results

Sample images for pre-exposure and post-atmospheric exposure are shown in Figure 27. No optically observable corrosion occurred on or near the shims, spot welds, or TC wires. No changes were observed to these materials over time. However, corrosion was observed on the 50 grit ground side of the SS316L plate. This can be further observed in Figure 27, where a) shows the mill finish surface, with obvious salt, but no corrosion, b) the weld region with salt, and only corrosion on the ground surface, and c) the ground surface and inset close-up of the shim. Additionally, it can be seen that while salt is present on the shim and wire, no enhanced corrosion was observed optically on either, only on the ground plate surface.

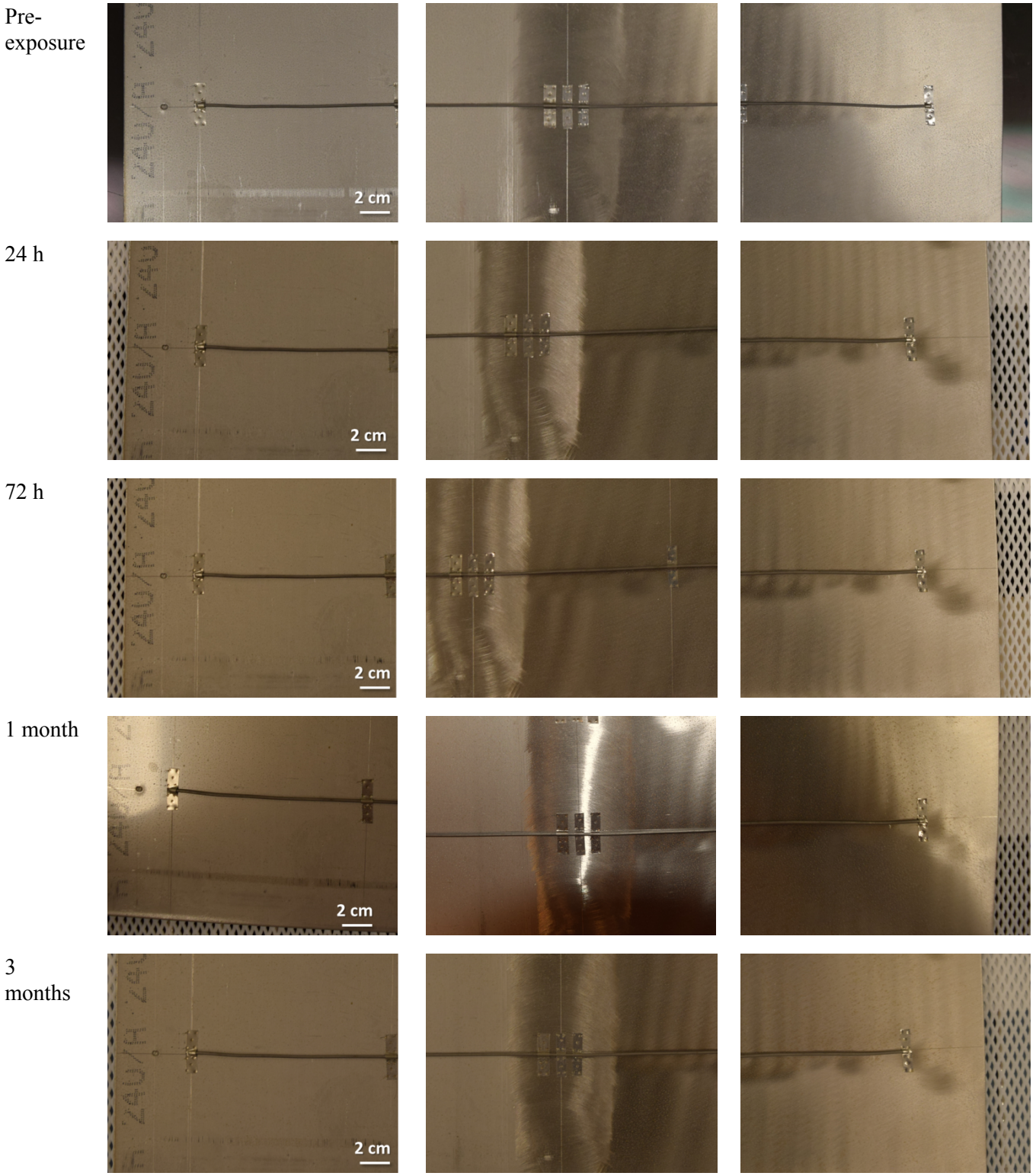

Figure 26. Select shim locations versus exposure time (left on mill scale, center in the weld, and right on ground surface).

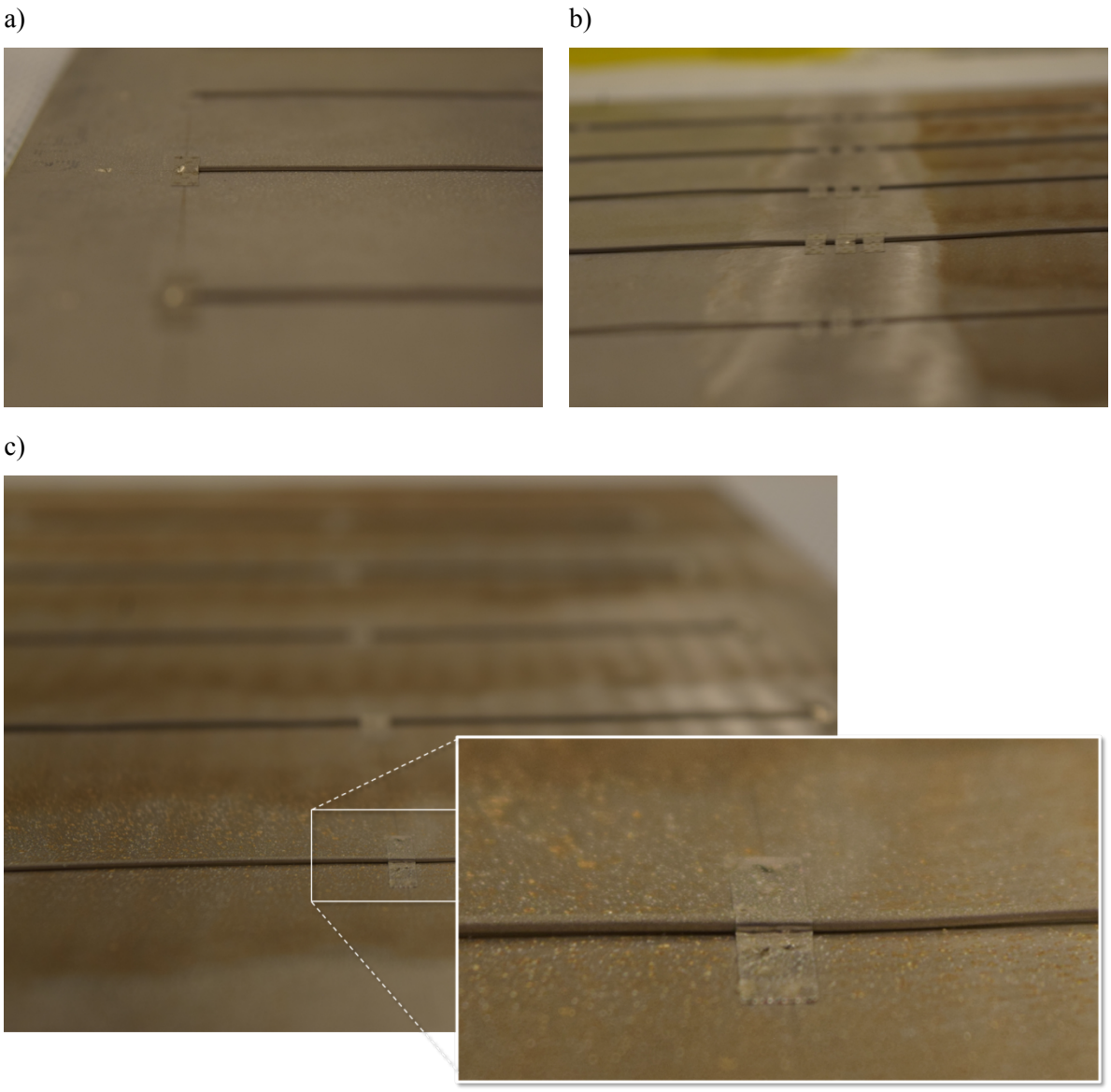

Figure 27. Representative shim locations after 3 months exposure for a) mill scale, b) within the weld, and c) rough grind. Images are angled to better view salt and potential corrosion product.

3.1.4 Future test plans and analysis for mockup plate

Over the course of the 3 months cyclic accelerated exposure, no corrosion was observed optically on the TC wires, shims, or spot welds. However, further analysis is required to definitively determine any potential detrimental effects that these materials might pose for the CDFD canister surface during longer term testing. Prior to termination of this test, collection of data over the following atmospheric exposures is proposed:

1) 1 month extension of current cyclic atmospheric exposure
2) After 1 month (4-month total exposure) additional salt deposition application (double current salt applied – 300 µg/cm^2 sea salt addition)

3) One month exposure in continued cyclic or static atmospheric exposure above NaCl deliquescence point to mimic potential conditions on unheated canister.
4) Continued image analysis at periodic time pulls
5) Post-1 month exposure (5-month total exposure) remove sample and prepare for post-mortem analysis (cut plate to sample sizes for Keyence, SEM, and profilometry analysis)
6) Perform pos-mortem analysis and relate potential ageing and lifetime observed to specific materials and methods applied to region of sample
7) Final analysis to be summarized in year-end report

4. TESTING OF HAND SAMPLING TECHNIQUES FOR QUANTITATIVE COLLECTION OF SAMPLE CANISTER SURFACE SALTS

During the CDFD project, the canisters will be pulled from the overpacks on a periodic basis, and the surface deposits will be collected by hand from the canister surfaces. Hand sampling is the preferred method for collection of dust and salts from the canisters because no validated robotic method exists. This is especially true for the unheated canister, on which the salts will be partially or fully deliquesced. Available robotic sampling methods utilize vacuum suction approaches to collect dry samples and will not be effective for very light salt loads, or for deliquesced brines that may adhere to the metal surface. A wet robotic sampling method has been used in the past but suffered from sampling a very small area, producing microgram-sized samples and making chemical analysis challenging. Additionally, this tool used in the previous wet sampling method is no longer commercially available. Another problem with existing robotic sampling methods is that the robot, traversing the canister surface and dragging its tether, would disturb surface dusts, interfering with future sampling plans. If carried out with care, hand sampling can be quantitative and will not disturb other regions on the canister surface.

For the CDFD project, the current plan is to place a series of 2 × 2 sample grids on the surface of each canister at 29 different locations, although some of the planned locations may not be accessible for sampling once the canisters are pulled out of the overpacks and onto a skid. For each sampling event, one or more of the grid squares will be sampled at each location. The squares are 76.2 mm on a side, so the area sampled is 58.06 cm^2. This large surface area increases the likelihood that collected salt concentrations will be large enough to be accurately quantified. To define and constrain the area that is being sampled, a plastic sampling mask will be pressed against the surface by hand, and the area within the mask will be sampled. A schematic of the mask is shown in Figure 28. The dust mask was fabricated using a Formlabs Form 3 photoreactive resin 3D printer using Formlabs' proprietary "Durable V2 Resin". The 3D print layer thickness was 100 microns. This resin was formulated to simulate the properties of polypropylene and has an ultimate tensile strength of 28 MPa, a tensile modulus of 1.0 GPa, and an elongation at break of 55% post-cure. Curing of the 3D printed part was achieved by baking in a Formlabs FormCure curing oven at 60°C for 60 minutes. The mask consists of two pieces that clip together, a handle and a base that outlines the 76.2 mm × 76.2 mm sample area. A polymer gasket is attached to the bottom of the sampler with an adhesive liner and will contact the canister surface to ensure a good seal. The handle is designed with high clearance to allow easy access to the sample region.

Because the same grid squares will be sampled more than once to get both specific time interval and cumulative deposition rates, it is important to be able to align the sampling tool exactly to the designated square within the sampling grid at each location; hence, the need for indexing marks as described in Section 3. Once aligned with the index marks, the tool will be pressed firmly against the canister surface and the surface deposits within the square will be quantitatively collected for analysis. Current plans call for use of damp sponges to collect the dust and salts from the canister surfaces. The sponges used will be ~1″ cubes of TruCLEAN® blue polyurethane sponge, moistened with deionized water; these sponges have been previously been used to collect dust and salts from SNF dry storage canisters, and have been confirmed to leach only very small amounts of soluble cations and anions [17]. In the case of heavy dust loads, the dust can be brushed into a small trough on one side of the sample region and then brushed or washed into a sample vial.

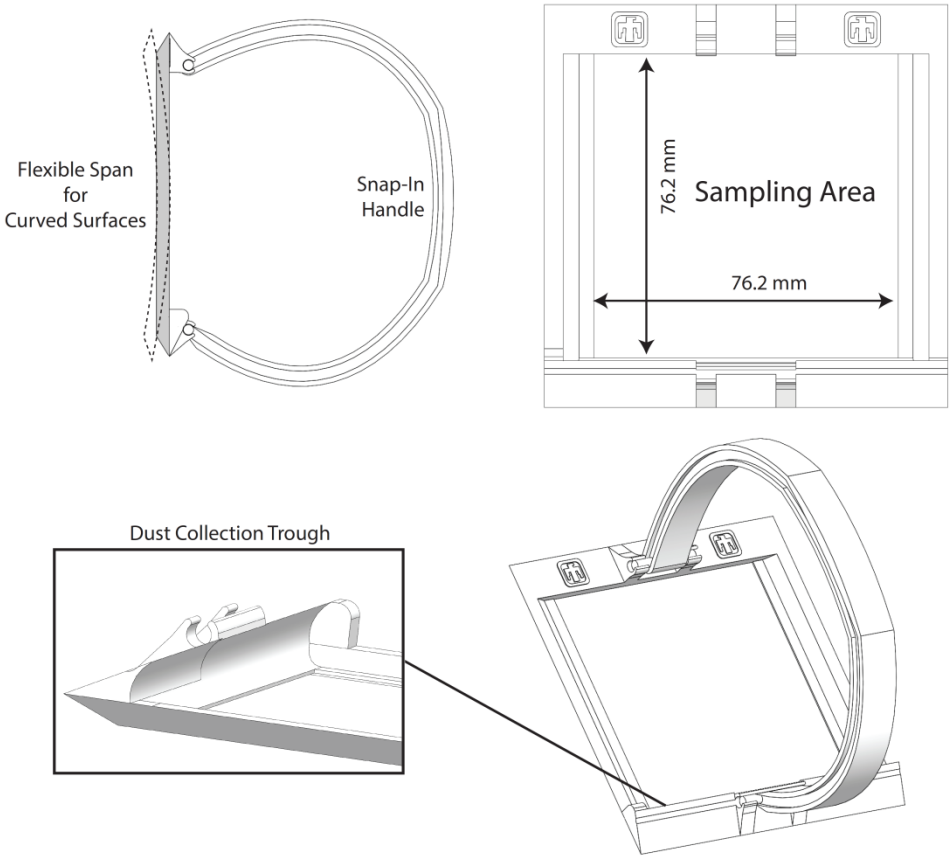

Figure 28. Dust sampling mask.

Laboratory tests are being performed to optimize the proposed approach and to verify that it results in quantitative recovery of all salts within the sampled area. To do this, a 20″ x 14″ plate of the Sandia mockup canister [7] was sampled. This plate has approximately the same curvature as a typical SNF dry storage canister and has a mill finish. Preparation of the plate is shown in Figure 29. First, the plate was thoroughly cleaned (Figure 29A) and a sampling grid with 3″ × 3″ squares was sprayed onto it (Figure 29B and Figure 29C) using an engine enamel. The engine enamel will not be used for marking the CDFD canisters as it does not withstand elevated temperatures, however for this test it was used while other the marking materials were evaluated. Then, several 1″ × 2″ stainless steel witness coupons were attached to the surface with conductive carbon tape (to minimize static issues when coating the plate with salts) surrounding the sampling grid (Figure 29D). The sample was then coated with ASTM sea salts using the previously mentioned SNL developed nebulizer system and approximately 200-300 µg/cm^2 sea-salts were deposited on the surface of the plate. Following salt deposition, the witness coupons were removed from the plate surface, transferred to sample vials, and leached with 20 mL of deionized water to extract the salts. The surface load varied with the location on the plate surface, but as simultaneous deposition was analyzed on the witness coupons through conductance measurements, the salt load was accurately mapped to determine how much salt was deposited within the squares of the sampling grid.

After removing the coupons, the dust sampling mask was pressed against the surface and the region within it was hand sampled using two 1″ cubes of the blue Tru-CLEAN sponges (Figure 30). For sampling, the sponges were wetted with deionized water and then gently squeezed to eject most of the water, leaving the sponge damp. The first sponge was used to wipe the surface and transferred to a 50 mL sample vial. Then, the second sponge was used to collect any remaining salts and added to the same vial.

40 mL of deionized water was added to each vial, and the sponges were repeatedly raised, compressed, and released with a steel spatula to equilibrate the fluid in the sponges with the bulk solution. For each test, two different personnel performed the sampling in an effort to evaluate person-to-person variability.

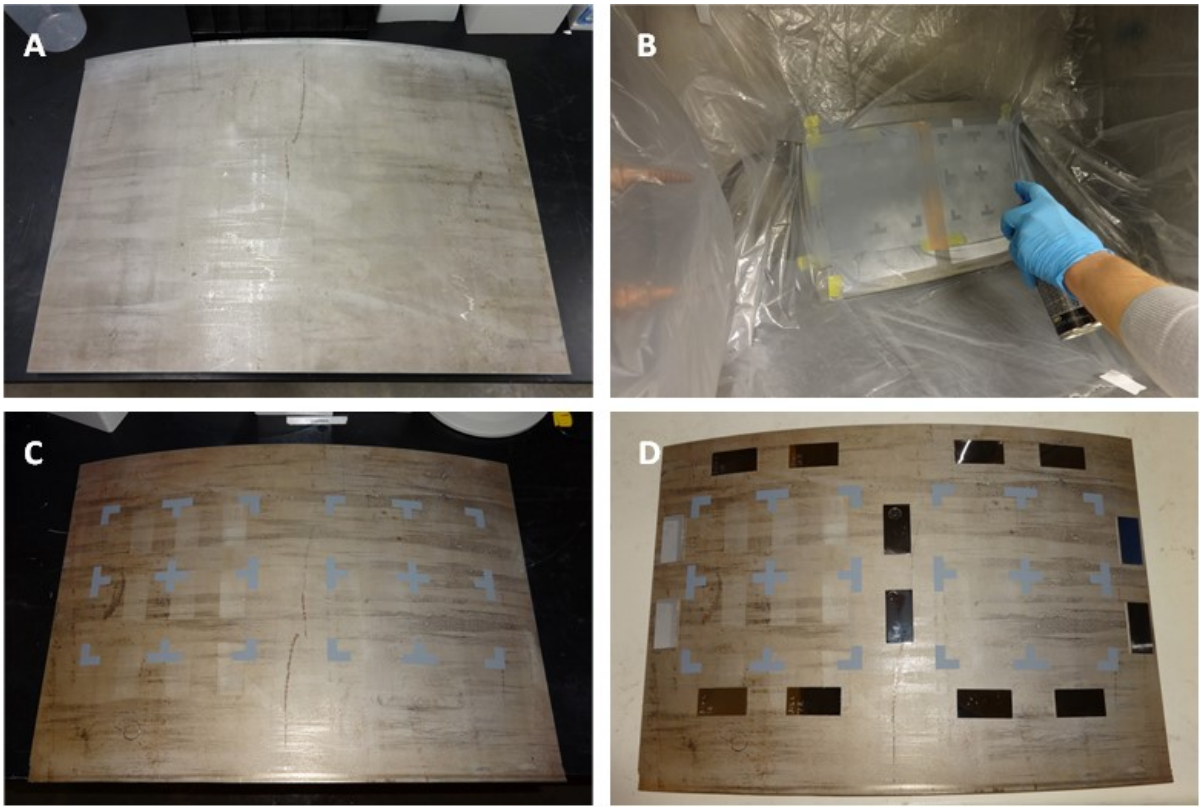

Figure 29. Preparation of the plate for dust sampling test. A—clean plate; B—spray-painting the grid onto the plate; C—the plate with sample grid; D—the plate with applied witness coupons.

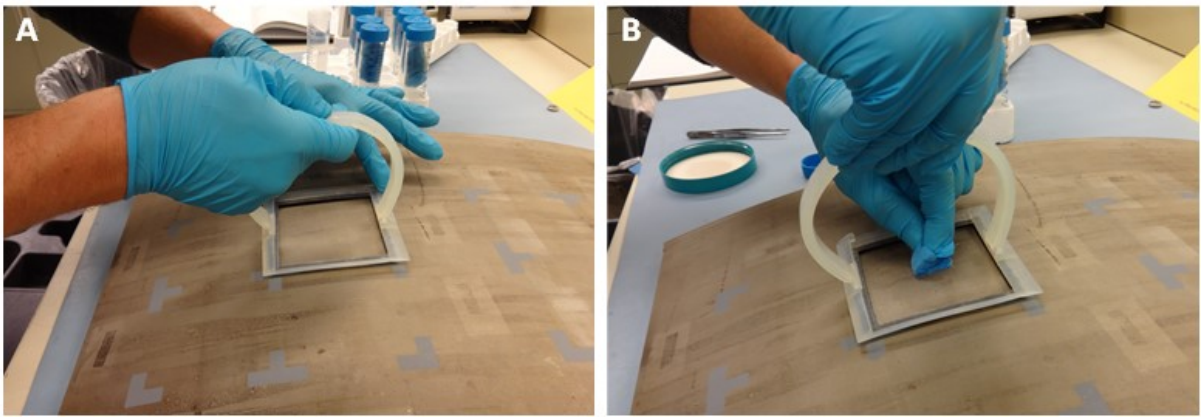

Figure 30. Sampling the deposited dust on the plate. A—dust sampling mask pressed to the metal surface; B—collecting salts with a moist sponge.

Following sampling, each of the witness coupon samples and grid samples were analyzed by measuring conductivity using a Jenway 4510 conductivity meter and a Jenway conductivity probe. Measured conductivities were normalized by the sampled area (2 in^2 for the witness coupons, and 9 in^2 for the grid cells) for comparison, yielding units of $\mu S/cm^2$. To determine what the salt loads were in the grid cells, the data for the witness coupons were fitted with a surface, and the deposit values at the grid centers were calculated by cubic interpolation (Figure 31). Although the nebulizer was generally effective, there was up to 25% variability in the salt load on the surface, with highest values trending across the center of the plate, below the path of the inlet flow from the nebulizer. Sampling efficiencies were calculated by comparing the measured salt loads for each grid square to those predicted by the surface fit to the witness coupon data and are shown in Figure 32. The estimated sampling efficiencies for the grid cells varied from -3.7% to -24.8%, but most were in the range of -10% to -15%. The low sampled values are attributed to incomplete recovery of the salts from the surface, either due to missing the edges and corners of the grid squares, or possibly due to the sponges not being sufficiently moist.

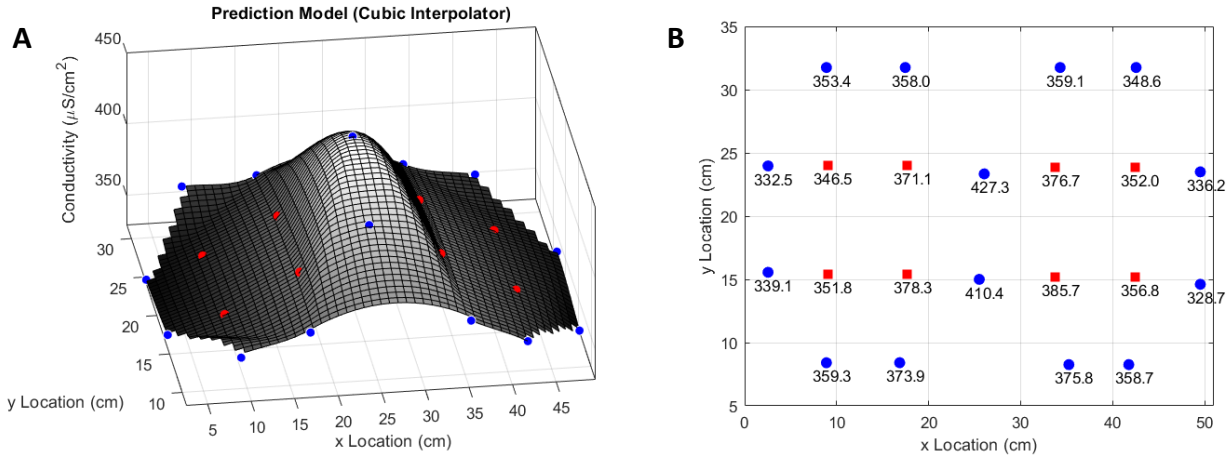

Figure 31. Test #1: fitting data from the witness coupons to determine expected salt load in the sample grid squares. A—fitted surface; B—measured witness coupon values (blue) and estimated grid cell values (red), $\mu S/cm^2$.

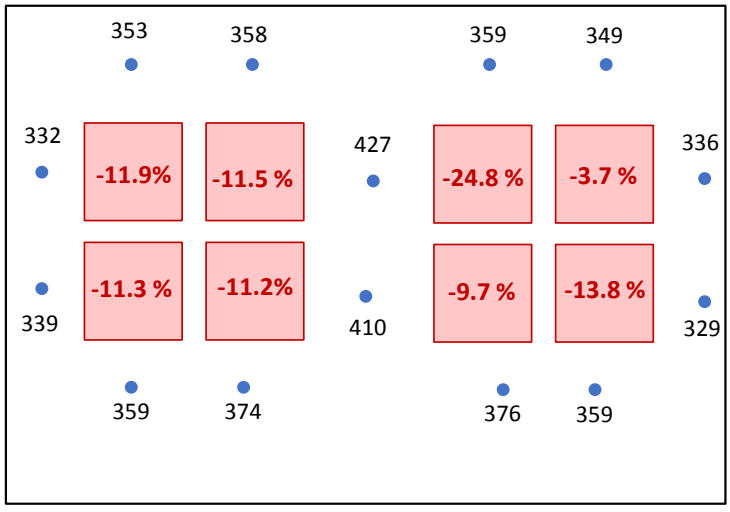

Figure 32. Test #1: Estimated sampling efficiencies for the 8 grid cells.

A second test was done using the same approach. However, results were highly variable, and resulted in significantly lower values in some cases. This was inconsistent with the increased care in sampling, and it was later discovered that variations in the sponge equilibration procedure were likely the cause. Those results are not shown here.

The third test incorporated several additional witness coupons to further capture the salt distribution on the plate, including small coupons in the center of each sampling grid. In addition, care was taken to ensure that the sponges were sufficiently moist during the sampling procedure. Finally, the sponges were thoroughly equilibrated with the added water after sampling. The results are shown in Figure 33 and Figure 34. As with the previous tests, the concentration of salts on the plate surface varied, with higher values along the axis of air flow within the nebulizer. Note that one of the small grid-center witness coupons (the right-side sample in Figure 33) proved difficult to remove from the plate, and upon analysis, contained a 20-40 μs/cm^2 higher salt load than the surrounding samples. It was assumed that this grid-center coupon was contaminated with additional salt during efforts to remove it from the plate surface, and it was not included when fitting the surface through witness coupon data. The estimated sampling efficiencies for the grid cells are shown in Figure 34. The sampled values varied from -2.4% to -8.2% of the values estimated from the witness coupons, much better that the first test. These values are considered acceptable if they can be achieved during sampling on the actual CDFD canisters.

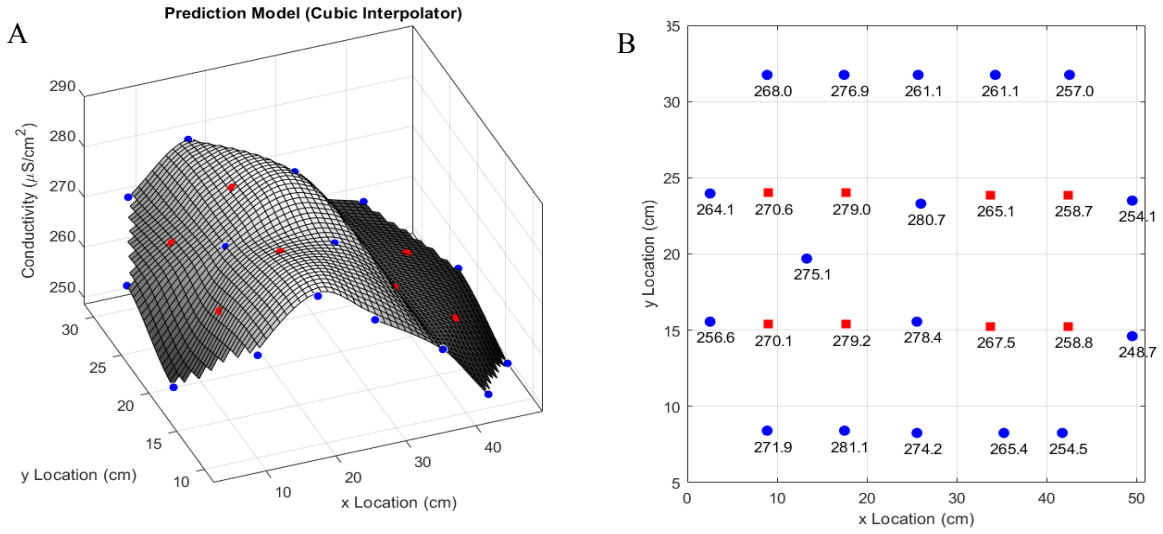

Figure 33. Test #3: fitting data from the witness coupons to determine expected salt load in the sample grid squares. Left—fitted surface; B—witness coupon and estimated grid cell values, μS/cm^2.

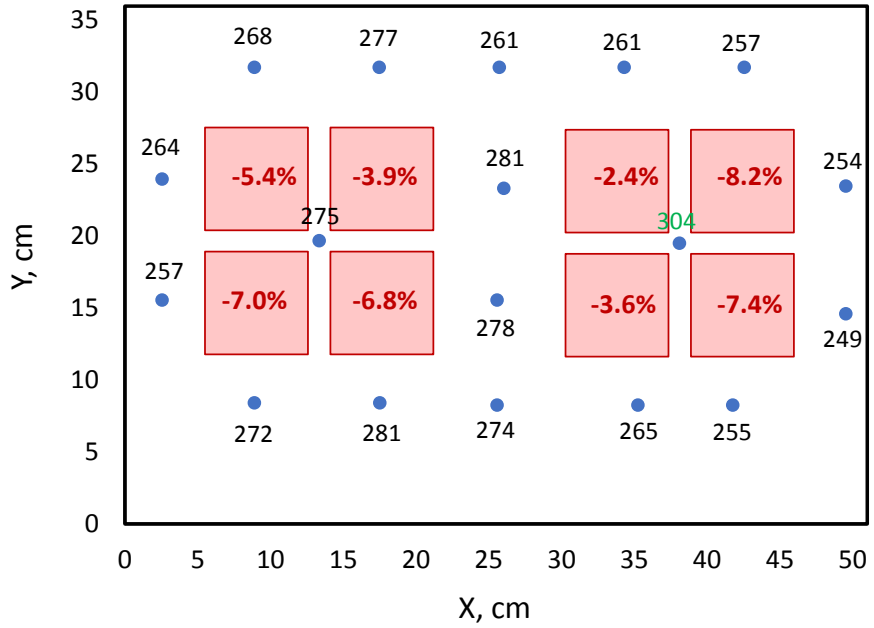

Figure 34. Test #3: Estimated sampling efficiencies for the 8 grid cells.

A fourth test yielded broadly similar tests to the third and is used here to illustrate that significant uncertainty in the sampling efficiency is caused by the overall testing method. In particular, the central witness coupons in each grid appear to vary significantly from the surrounding grid cells and samples. In part, this may be because the central coupons are smaller (1″ square) that the other witness coupons, that are 1″ x 2″. This means that any errors in the measured salt load on the central coupons are magnified relative to the other coupons. The smaller size also means that it is more difficult gently pry the central coupons to pry them off the plate, potentially increasing the chance of contamination during the sampling process. In the fourth test, both of the central samples varied significantly from the surrounding samples, one being slightly lower, and the other much higher. Including of excluding these points significantly affects the predicted concentrations in the sampled grid blocks, and hence, the predicted sampling efficiency. The results are shown in Figure 35 and Figure 36 for the case when both central points were included, and in Figure 37 and Figure 38 when neither was included. It is clear that the measured deposited salt load at the right center point is much larger than for nearby witness coupon and is inconsistent with the general trends in the data. Including the right-center point results in much higher predicted salt densities in the right-hand sample grid, and compared to the actual measured grid concentrations, predicts that the salt load was under-sampled by 10-15%. Leaving this sample out seems justified, because of the large difference relative to the other witness coupons, and results in predicted sampling efficiency in the right-hand grid of >90%. The left enter point is only slightly low relative to the surrounding points but keeping it or removing it significantly affects the apparent sampling efficiency. In this case, keeping the center point results in a better predicted sampling efficiency, while removing it results in a worse sampling efficiency. Even considering these uncertainties, however, the measured sampling efficiencies are broadly consistent with the results form Test #3, and indicate better than 90% salt recovery.

In each of the three later sampling tests, the grid-center witness coupons differed significantly from the surrounding coupons and the sampled squares within the grids, and account for a significant fraction of the uncertainty associated with the sampling procedure. We speculate that this is due to static charging issues with the grid-center coupons. Although attached to the plate with the plate with the same conductive carbon tape as the other coupons, the grid-center coupons are actually attached to the engine

enamel gird lines, instead of to the bare metal. Hence, they may be electrically isolated from the plate itself and subject to static buildup. In future tests, the effect of grounding these coupons to the bare metal will be evaluated.

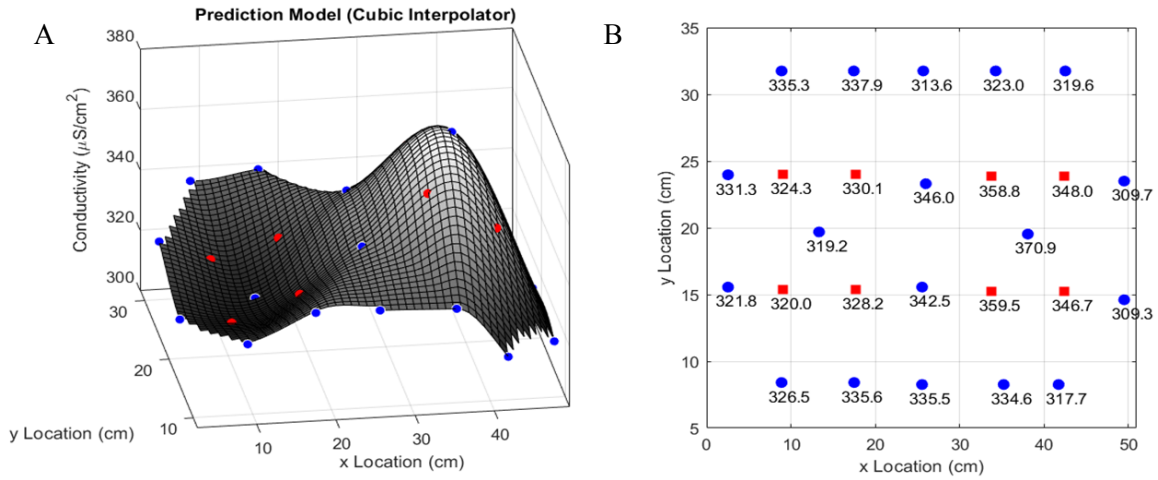

Figure 35. Test #4, central grid points included: fitting data from the witness coupons to determine expected salt load in the sample grid squares. Left—fitted surface; B—witness coupon and estimated grid cell values, μS/cm².

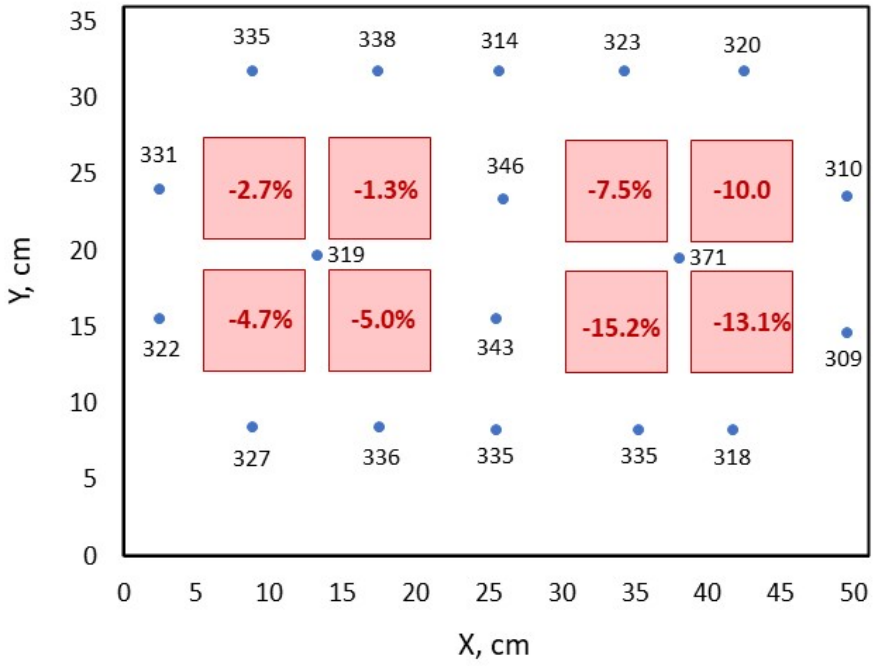

Figure 36. Test #4, central grid points included: Estimated sampling efficiencies for the 8 grid cells.

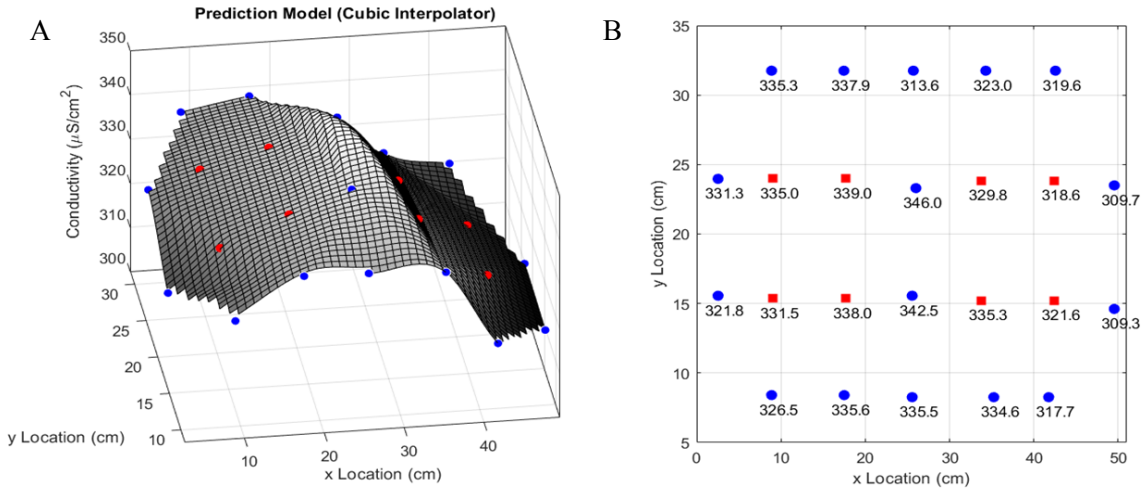

Figure 37. Test #4, central grid points excluded: fitting data from the witness coupons to determine expected salt load in the sample grid squares. Left—fitted surface; B—witness coupon and estimated grid cell values, μS/cm².

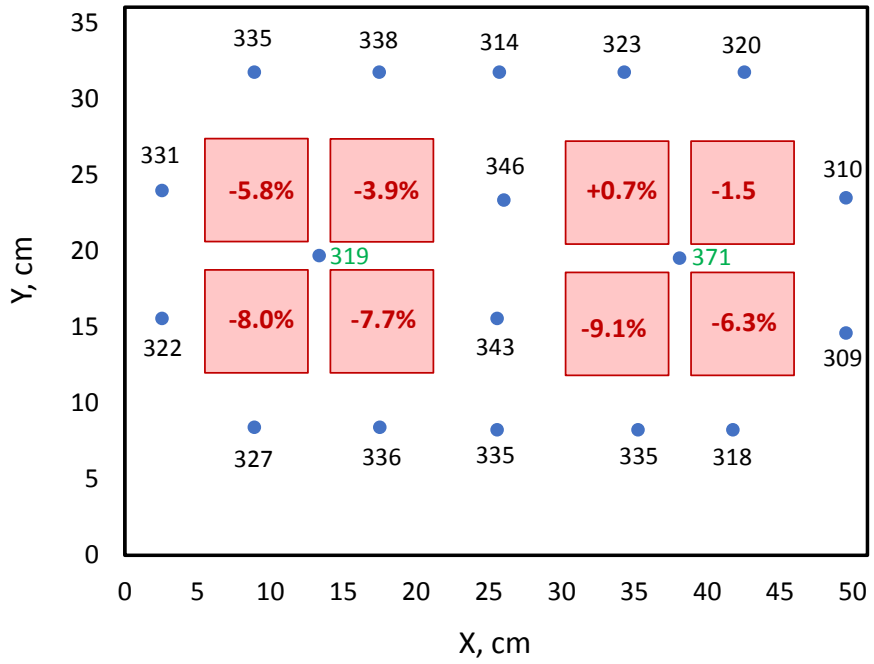

Figure 38. Test #4, central grid points excluded: Estimated sampling efficiencies for the 8 grid cells.

Additional tests will be carried out to verify these efficiencies, to test the method on vertical metal surfaces, and to evaluate other potential methods for further improvement. A field test on a real canister or a larger scale mockup will also be carried out to evaluate the feasibility of the applying the hand-sampling procedure to vertical and overhanging canister surfaces while on a lift; however, this logistical test will not involve deposition of salts onto the metal surface.

5. CONCLUSIONS

This report provides initial testing details regarding canister surface sampling for the CDFD project to assess and evaluate the salt deposition of three full scale 32PTH2 NUHOMS welded SS SNF canisters. For the CDFD project, canisters heat loads were designed to simulate the canister surface temperatures corresponding to ambient conditions and two different fuel heat loads (0 kW, 10 kW, and 40 kW), and will be periodically sampled on a yearly or bi-yearly basis over the course of the multi-year experiment. A previous report from FY21 summarized the proposed sampling locations and frequency [1], and this report describes initial tests to evaluate the surface sampling techniques. Here we measure the variability of the canister surface roughness via profilometric analysis of surface replicating molds. We demonstrated that the normal surface roughness corresponds to about 180-grit surface finish and identified the roughness of several other canister features. The weld and HAZ regions had measured surface roughness that were rougher than the normal surface roughness, which could play a role in their susceptibility toward localized corrosion. In addition to surface roughness, we quantified the size of mechanically formed pits found on the surface and demonstrated that the majority of these pits had a very small aspect ratio. This surface roughness information may be used to identify if deviations in surface roughness impact the dust and salt deposition on the canister. The ageing and lifetimes of the TC wires, attachments, and spot welds were evaluated to assess their impact on canister corrosion during the CDFD project. These materials were tested in an accelerated cyclic atmospheric environment and exposed for 3-months thus far. To date, no corrosion has been observed optically on the TC wires, attachments, or spot welds, or on the mill finish side of the SS plate, however some corrosion has been observed on the rougher surface. These experiments will continue for several more months and effort will be made to accelerate the aggressive environment (e.g. increase salt load and increase relative humidity) in order to increase confidence that these materials will not negatively impact canister corrosion over the course of the CDFD campaign (especially for the 0 kW canister case). Lastly, we tested our surface sampling method using the surface sampling template and Tru-CLEAN sponges to quantitatively recover all the salt form a given surface. To date, we have performed 3 tests and evaluated our ability to recover the salts from the surface. Improvements were made in the methodology from Test 1 (e.g. more efficient at removing salt from corners) and Test 2 (e.g. ensure effective salt leaching of the sponges) to maximize our recovery from Test 3, where the recovery ranged +0.7%- -5.3% and fell within an acceptable range. Additional verification tests will be performed to continue to instill confidence in the hand sampling method.

The tests performed in this report lay the foundation for surface sampling efforts during the CDFD campaign, targeted to improve our understanding of dust deposition on SNF canisters. While several coastal [18-20] and inland [21, 22] independent spent fuel storage installations have been sampled, the sampling efficiency of the robotic sampling performed at these sites is unknown, thus the salt load is not quantitative. The validation of a sampling method is critical to in order to determine quantitative salt loads and therefore the methods described in this report will help provide the critical information needed to parameterize and validate the dust deposition models that are being developed at PNNL [23, 24]; provide input conditions for representative corrosion studies; and aid in the efforts to develop a better understanding of the potential risk of SCC of SNF dry storage canisters.

6. REFERENCES

1. Bryan, C., et al., *Surface Sampling Techniques for the Canister Deposition Field Demonstration*. 2021, Sandia National Laboratories: Albuquerque, NM.

2. Bryan, C., et al., *FY21 Status Report: SNF Interim Storage Canister Corrosion and Surface Environment Investigations*. 2021, Sandia National Laboratories: Albuquerque, NM. p. 199.

3. Tanbakuchi, A., *Photometrics Report: Cylinder Image Mapping*. 2021, Sandia National Laboratories: Albuquerque, New Mexico.

4. Novak, A.H. and B. Runje, *Incfluence of Object Surface Roughness in CT Dimensional Measurements*, in *7th Conference on Industrial Computed Tomography*. 2017: Leuven, Belguim.

5. Dashti, M. and A. Abdulaziz, *A Review on Surface Roughness (Ra) Ranges for Some Finishing Processes.* International Journal of Scientific and Engineering Research, 2020. **11**(4).

6. Whitehorse, D., *Surfaces and Their Measurement* 1st ed. 2004, Boston, MA: Butterworth-Heinemann.

7. Enos, D. and C. Bryan, *Final Report: Characterization of Canister Mockup Weld Residual Stresses*. 2016, U.S. DOE. p. 62.

8. *Advanced NUHOMS System Updated Final Safety Analysis Report*. 2016.

9. *Grit Size vs. Surface Roughness*. 2018 04/07/2022]; Available from: https://www.engineeringtoolbox.com/grit-size-surface-roughness-d_2096.html.

10. Cerit, M., *Corrosion pit-induced stress concentration in spherical pressure vessel.* Thin-Walled Structures, 2019. **136**: p. 106-112.

11. Chen, Z.Y. and R.G. Kelly, *Computational Modeling of Bounding Conditions for Pit Size on Stainless Steel in Atmospheric Environments.* Journal of The Electrochemical Society, 2010. **157**(2): p. C69.

12. Katona, R.M., et al., *Prediction of Maximum Pit Sizes in Elevated Chloride Concentrations and Temperatures.* Journal of The Electrochemical Society, 2019. **166**(11): p. C3364-C3375.

13. Katona, R.M., et al., *Quantitative assessment of environmental phenomena on maximum pit size predictions in marine environments.* Electrochimica Acta, 2021. **370**: p. 137696.

14. Weirich, T.D., et al., *Humidity Effects on Pitting of Ground Stainless Steel Exposed to Sea Salt Particles.* Journal of The Electrochemical Society, 2019. **166**(11): p. C3477-C3487.

15. Hong, T. and M. Nagumo, *Effect of surface roughness on early stages of pitting corrosion of Type 301 stainless steel.* Corrosion Science, 1997. **39**(9): p. 1665-1672.

16. Burnstein, G.T. and P.C. Pistorius, *Surface roughness and the metastable pitting of stainless steel in chloride solutions.* Corrosion 1995. **51**(5): p. 380-385.

17. Bryan, C. and D. Enos, *Analysis of Dust Samples Collected from an In-Service Interim Storage System at the Maine Yankee Nuclear Site*. 2016, Sandia National Laboratories: Albuquerque, NM. p. 51.

18. Bryan, C. and E. Schindelholz, *Analysis of Samples Collected from the Surface of Interim Storage Canisters at Calvert Cliffs in June, 2017: Revision 01*. 2017, Sandia National Laboratories Albuquerque NM.

19. Bryan, C. and D. Enos, *Anlaysis of Dust Samples Collected from Spent Nuclear Fuel Interim Storage Canisters at Hope Creek, Delaware, and Diablo Canyon, California*. 2014, Sandia National Laboratory: Albuquerque, NM.

20. Bryan, C. and D. Enos, *Analysis of Dust Samples Collected from an Unused Spent Nuclear Fuel Interim Storage Container at Hope Creek, Delaware*. 2015 Sandia National Laboratories: Albuquerque, NM

21. Knight, A.W. and C. Bryan, *Analysis of Dust Samples Collected from an Inland ISFSI Site ("Site B")*. 2020, Sandia National Laboratories: Albuquerque, New Mexico

22. Bryan, C. and A.W. Knight, *Analysis of Dust Samples Collected from an Inland ISFSI Site ("Site A")*. 2020, Sandia National Laboratories: Albuquerque, New Mexico

23. Jensen, P., S.R. Suffield, and B. Jensen, *Status Update: Depostion Modeling For SNF Canister CISCC*. 2020: U.S. Department of Energy. p. M3SF-21PN01020705/M3SF-20PN102070412.

24. Jensen, P., et al., *Preliminary Depostion Modeling: For Determining the Depostion of Corrosive Contaminants on SNF Canisters*. 2020: U.S. Department of Energy. p. MS3SF-20PN010207045.

This page is intentionally left blank